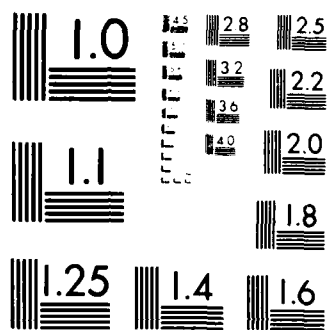MONOLITHIC THIN FILM SAW (SURFACE ACOUSTIC WAVE)
STRUCTURES(U) PURDUE UNIV LAFAYETTE IN SCHOOL OF
ELECTRICAL ENGINEERING R L GUNSHOR ET AL. 01 SEP 84

UNCLASSIFIED AFOSR-TR-84-1235 AFOSR-83-0237   F/G 9/5   NL

END

MICROCOPY RESOLUTION TEST CHART

NATIONAL BUREAU OF STANDARDS 1964 A

AFOSR-83-0237
Interim Scientific Report
1 September 1984

AD-A149 782

MONOLITHIC THIN FILM SAW STRUCTURES

R. L. Gunshor, S. Datta, and R. F. Pierret

School of Electrical Engineering
Purdue University
West Lafayette, Indiana 47907

DTIC
ELEC
JAN 2 4 1985

85 01 15 024

REPORT DOCUMENTATION PAGE

1 REPORT NUMBER	
AFOSR	

4 TITLE (and Subtitle)

Monolithic Thin Film SAW Structures

7 AUTHOR(s)

R. L. Gunshor, S. Datta, and R. F. Pierret

8 CONTRACT OR GRANT NUMBER

AF

9 PERFORMING ORGANIZATION NAME AND ADDRESS

School of Electrical Engineering
Purdue University
West Lafayette, IN 47907

10 PROGRAM ELEMENT, PROJECT, TASK AREA & WORK UNIT NUMBERS

11 CONTROLLING OFFICE NAME AND ADDRESS

Air Force Office of Scientific Research
Building 410
Bolling AFB, D.C. 20332

12 REPORT DATE

September

13 NUMBER OF PAGES

14 MONITORING AGENCY NAME & ADDRESS(if different from Controlling Office)

SAME

15 SECURITY CLASS (of this report)

15a DECLASSIFICATION DOWNGRADING SCHEDULE

16. DISTRIBUTION STATEMENT (of this Report)

Approved for public release; distribution unlimited.

17. DISTRIBUTION STATEMENT (of the abstract entered in Block 20, if different from Report)

SAME

18 SUPPLEMENTARY NOTES

N/A

19 KEY WORDS (Continue on reverse side if necessary and Identify by block number)

Surface acoustic waves, ZnO, GaAs, AlGaAs, piezoelectric device, storage correlators, resonators.

20 ABSTRACT (Continue on reverse side if necessary and Identify by block number)

A review of storage correlation is presented. The homogeneous and

tures are proposed.

RESEARCH OBJECTIVES

Introduction

The research effort reviewed in this report reflects a transition in specific objectives, while continuing to be directed at the development of monolithic microwave acoustic structures. Although considerable progress has been achieved at frequencies of up to a few hundred MHz, little or nothing is known of the behavior of thin film monolithic devices at microwave frequencies (above 1Ghz). The emphasis of the research program, therefore, has been shifted to the exploration of the limits of several materials and configurations at higher frequencies with the objective of determining the dominant factors (such as the relationship between propagation loss and film microstructure) which act to limit device performance. The change in emphasis is greatly facilitated by the installation of a high resolution electron beam lithography system; the installation is to be completed in the month of November 1984. At the same time we have greatly increased the sophistication of our materials preparation and characterization capability through our involvement in the growth of films by molecular beam epitaxy. Routine collaborations with Professor N. Otsuka has added high resolution (3Å) transmission electron microscopy to our capability. The information resulting from interface imaging is expected to prove critical in the preparation of very thin (dictated by higher frequencies) oriented piezoelectric films.

Finally it is important to observe that although SAW devices have developed into a mature technology for high speed signal processing in the 50-500 MHz range, they have had only a tenuous connection to the areas of integrated electronics and integrated optics. We perceive two main reasons why a widespread integration has not occurred despite the obvious motivation:

1. Incompatibility of substrates: SAW technology is centered around lithium niobate and quartz, while integrated electronics is based on silicon and gallium arsenide, with integrated optics involving lithium niobate and gallium arsenide.

2. Incompatibility of dimensions: The wavelengths used in SAW devices are typically 10-30 μm; these values are large compared to the dimensions associated with either integrated electronics or optics.

To overcome these inherent problems we are proposing a novel and unique approach using high frequency (1GHz and above) guided acoustic waves in an AlGaAs-GaAs-AlGaAs structure. The initial effort, commencing during the current reporting year, is described in section A of this report.

Specific Results

A. Double heterostructure Waveguides

Our most recent work involves studies of an AlGaAs-GaAs-AlGaAs structure. AlGaAs has an acoustic wave velocity which is 20 to 25% higher than GaAs. As a consequence, an acoustic wave can be guided along the buried GaAs layer. These waves have the following attractive features:

1. Substrate compatibility: integrated electronics and integrated optics are both centered around GaAs.

2. Dimensional compatibility: the acoustic energy resides in a buried layer away from the surface. The scattering losses associated with the surface are minimized, and it should be possible to propagate acoustic waves with frequencies exceeding 1GHz; losses due to the interface are expected to be minimal, since light waves with similar wavelengths are known to propagate well in these structures. The associated acoustic wavelengths are 1μm or less, and hence compatible to typical optical wavelengths.

3. Compatibility of Configuration: In an AlGaAs-GaAs-AlGaAs both acoustic and optical waves are guided along the GaAs layer so that large acousto-optic interactions should be possible. Moreover, MODFET's which are becoming increasingly popular also use exactly the same structure.

We believe that the possibility of using the same identical structure for integrated electronics, optics and acoustics is rather unique and this can lead to a whole new field of *integrated acoustics* which will be compatible with both integrated electronics and integrated optics. A true integration of these technologies could have a significant impact on both the areas of acousto-optics and acousto-electronics.

3. Implanted Isolated Storage Correlator

During the past year a new configuration for a monolithic storage correlation was conceived, constructed, and tested. The new device is called an Implant Isolated Storage Correlator and utilizes an ion-implanted array to isolate sampled signal storage regions. The device is simple to fabricate, requiring neither pn or Schottky diode arrays for signal storage. The memory function is accomplished through alteration of depletion widths of MOS induced junctions with storage times longer than previous

monolithic configurations. A complete description of the implant isolated memory correlator is found in the preprint manuscript for the *invited paper* included as Appendix A.

C. Theory For Perturbations in Layered Media

Appendix B contains a copy of the *invited paper* delivered at the 1983 IEEE Ultrasonics Symposium. This work represents the first computation for the prediction of wave reflection and Rayleigh-Sezawa mode conversion produced by ion-milled grooves in monolithic thin film acoustic devices. The theoretical estimates conform closely to experimental measurements. Further details concerning the theory of mode conversion produced by grooved arrays in layered media are given in the report of our article in the Journal of Applied Physics (Appendix C).

D. Mode Conversion Resonator

Theoretical considerations related our recently proposed mode conversion resonator have led to predictions of a SAW resonator whose transducer position in the cavity is not a critical design parameter. This rather surprising result has important implications for the fabrication of SAW resonators, as critical alignment steps can be eliminated. Furthermore, the grooved reflector array and aluminum transducer can be defined in separate fabrication steps; an advantage not possible with previous SAW resonators. Mode conversion resonators utilizing this relaxed spacing requirement are being examined in both one and two port configurations. The initial results of this effort will be presented at the 1984 IEEE Ultrasonics Symposium.

E. High Q Resonators

During the past year we addressed the problem of achieving Q values for the on-silicon resonators which are greater than the 12,000 we previously reported. Since the ZnO layer contributes to the propagation loss, and hence to a reduction in Q, we have fabricated externally coupled resonators with ZnO limited to the regions of transduction. in the externally coupled device configuration resonant at 110 MHz we obtained Q values of 25,900 for propagation on SiO2-Si, and up to 31,400 for propagation on unoxidized silicon. Details of this work were reported at the 1983 IEEE Ultrasonics Symposium, and the Proceedings paper is included as Appendix D. We are currently involved in the fabrication of high-Q, ZnO-limited resonators in an internally coupled resonator configuration.

PUBLICATIONS

S. Datta and R. L. Gunshor, "Space Charge Waves in Multilayered Heterostructures," Journal of Applied Physics 54, 4453 (1983).

S. Datta, "Reflection and Mode Conversion of Surface Acoustic Waves in Layered Media," Invited Paper presented at the IEEE Ultrasonics Symposium, Atlanta, 1983.

S. S. Schwartz, S. J. Martin, R. L. Gunshor, S. Datta, and R. F. Pierret, "SAW Resonators on Silicon with ZnO Limited to IDT Regions," presented at the IEEE Ultrasonics Symposium, Atlanta, 1983.

S. J. Martin, R. L. Gunshor, M. R. Melloch, S. Datta, and R. F. Pierret, "Surface Acoustic Wave Mode Conversion Resonator," Applied Physics Letters, 43, 238 (1983).

S. Bandyopadhyay, S. Datta, S. J. Martin, and R. L. Gunshor, "Coherent Mode Conversion by Grooved Arrays in Layered Media," Journal of Applied Physics, 55 69 (1984).

S. S. Schwartz, S. J. Martin, R. L. Gunshor, S. Datta, and R. F. Pierret, "SAW Resonators Insensitive to IDT Position," to be presented at the IEEE Ultrasonics Symposium, Dallas, 1984.

S. S. Schwartz, R. L. Gunshor, and R. F. Pierret, "Implant-Isolated SAW Storage Correlator," Invited Paper to appear in IEEE Transactions on Sonics and Ultrasonics, June 1985.

PERSONNEL

Robert L. Gunshor, Professor of Electrical Engineering;
Supriyo Datta, Associate Professor of Electrical Engineering:
Robert F. Pierret, Professor of Electrical Engineering
Stephen S. Schwartz, Graduate Research Assistant
Stephen J. Martin, * Graduate Research Assistant
Larry Pearce, ** Graduate Research Assistant
Mike Church, ** Graduate Research Assistant
Supriyo Bandyopadhyay, Graduate Research Assistant
Biswajit Das, Graduate Research Assistant
Timothy J. Miller, Technician

DEGREES AWARDED

Stephen J. Martin, Ph.D., "Zinc Oxide-on-Silicon Surface Acoustic Wave Resonators,"
December 1983.

Lawrence G. Pearce, Ph.D., "Reactive RF Magnetron Sputtered Aluminum Nitride on
Silicon for Surface Acoustic Wave Device Applications," May 1984.

PATENT AWARDED

U.S. Patent 4,437,031 (March 13, 1984), ZnO SAW Device Having Separate Comb
Transducer, R. L. Gunshor, R. F. Pierret, and Michael R. Melloch.

PATENT APPLICATION

Surface Acoustic Wave Mode Conversion Resonator, R. L. Gunshor, S. J. Martin, M.
R. Melloch, (filed December 7, 1983).

---

* Currently at Sandia National Laboratory.
** Currently at Harris Semiconductor Corporation

APPENDIX A

IMPLANT-ISOLATED SAW STORAGE CORRELATOR

S. S. Schwartz, R. L. Gunshor, and R. F. Pierret

School of Electrical Engineering, Purdue University,

West Lafayette, In. 47907

ABSTRACT

The development of surface acoustic wave (SAW) convolvers and correlators is first reviewed. This is followed by the introduction of a new type of monolithic metal-zinc oxide-silicon dioxide-silicon storage correlator. Fabrication and operation of the implant isolated storage correlator, which relies on ion implantation for confinement of storage regions, is next detailed. A capacitance-time measurement procedure for evaluation of the charge storage capability of the device is described, and correlation output information is used to estimate the effective recombination rate of the inversion layer charges. Finally, operational characteristics are examined and the new bias stable device is shown to exhibit a 3 dB storage time in excess of 0.5 seconds. The cited storage time exceeds reported storage times of other structures fabricated in the $ZnO/SiO_2/Si$ layered medium configuration.

I. INTRODUCTION

Surface acoustic wave convolvers and memory correlators are devices which utilize the nonlinear interaction of the electric field associated with acoustic waves in a piezoelectric medium to perform real time multiplication of two signals. A representative monolithic metal–piezoelectric film–SiO_2–Si convolver is shown in Fig. 1. The piezoelectric layer enables one to excite surface acoustic waves in the silicon by applying rf signals to interdigitated transducers on the surface of the substrate. The electric field pattern produced by fingers of alternating polarity induce periodic time and spatial stresses in the piezoelectric layer, thereby exciting a surface acoustic wave. Associated with each propagating surface wave is an accompanying electric field. It is the nonlinear interaction within the semiconductor between the electric field patterns of two contra-propagating waves that produces a signal proportional to the product of the two acoustic signals at every point in the device. The function of the third electrode, known as the gate, is to sum the product signal over the length of the device. When two signals are applied simultaneously to the two transducers, the output at the gate is proportional to the time-compressed convolution of the two signals.

The development of monolithic SAW devices has emphasized the use of ZnO and AlN as piezoelectric films. Although ZnO has received the most attention, AlN[1,2] has some attractive features related to ruggedness and the potential for low dispersion. Both materials can be utilized to achieve a temperature stable configuration.

It should be noted that the Fig. 1 configuration is but one of several ways

to realize the piezoelectric-semiconductor interaction. For example, a separated medium technique has been employed where a semiconductor (Si) and a bulk piezoelectric crystal (usually LiNbO$_3$) are mounted in close proximity[3,4,5,6,7,8]. The separated medium structure, although mechanically more complex than a monolithic configuration, has a wide bandwidth capability[9] as a result of the high electromechanical coupling coefficient of LiNbO$_3$. To increase the bandwidth capability of devices fabricated in the monolithic ZnO/SiO$_2$/Si system, thereby making them more attractive as practical signal processing devices, higher electromechanical coupling was sought by employing a higher order Rayleigh mode. It has been shown that the second order or Sezawa mode of the layered ZnO/SiO$_2$/Si configuration can be efficiently excited in high quality films[10]. The electromechanical coupling coefficient available from this mode exceeds that for Rayleigh waves in bulk ZnO, and is close to the value for LiNbO$_3$. Several convolvers and diode storage correlators which exploit the bandwidth advantage of the Sezawa mode have been reported[11,12,13,14].

Convolvers, it should be pointed out, can be used to perform correlation between two signals. A disadvantage of correlating two signals using a convolver is that the reference signal must be time reversed An electronic time reversal technique[15] has been demonstrated in a convolver system[16], but at a sacrifice of high insertion loss which leads to a degraded dynamic range. Additionally, an incoming signal arriving at an unknown time necessitates repeated application of the reference signal to counter the uncertainty of the arrival time which in turn leads to a smaller effective time-bandwidth product.

The storage correlator is a device which performs both convolution and correlation without the need for time reversal and without concern for the uncertainty of the arrival time of the signal to be interrogated. Hence, two of the major drawbacks of performing correlation with the convolver system are eliminated by utilizing a memory correlator.

A simplified description of the storage correlation process can be given with the aid of Fig. 2 which depicts a typical memory correlator. Under normal operation, one introduces a signal at one of the transducers such that a sampled version of this reference signal, $S(t)$, is stored beneath the gate of the device by one of several possible writing procedures. At some later instant, but still within the storage time of the reference signal, a second signal, $R(t)$, is applied to the gate of the correlator. The introduction of $R(t)$ at the gate electrode excites two contra-propagating signals representing the product of $R(t)$ and $S(t)$, which subsequently appear at the two output transducers; it can be shown that the correlation appears at one transducer, while the convolution output is available at the other.

To date, several memory array configurations have been employed in the fabrication of storage correlators. Schemes for signal storage by means of surface states[17,18], pn diodes[19,20,12,21,22], and Schottky diodes[23,24,25] have been examined. More recently, a new type of junction storage correlator has been introduced[26] in which the spatial variation of inversion layer charge at the SiO_2/Si interface of the ZnO monolithic configuration has been utilized for signal storage. With the exception of this "induced junction" storage correlator, the various storage schemes have been employed in both monolithic and separated medium configurations.

The first memory devices utilized semiconductor surface states for signal storage[17,18]. In a surface state memory correlator, the electric field pattern associated with an applied signal causes a bunching (periodic spatial concentration) of free electrons at the Si/SiO_2 interface. Subsequently, a portion of the electrons are trapped at the interface thereby producing a spatially varying charge pattern. The storage time of these devices corresponds to the detrapping time which is a function of the properties of the interface. Surface state storage was subsequently replaced by more easily controlled and repeatable diode storage arrays. More recently, reference signal storage in induced junctions was reported[26]. In both diode and induced junction array processes, the principle of charge storage is essentially the same. Recombination of minority carriers injected out of a p^+ region (or inversion layer in the case of the induced junction device) by an applied signal causes an alteration of the diode (induced junction) depletion width.

The monolithic metal/ $ZnO/SiO_2/Si$ (MZOS)[27,28] memory correlator introduced this paper utilizes depletion regions in the silicon to store a reference signal, but in an MOS region of n-type silicon only; that is, no diodes or surface states are employed for storage. Furthermore, the uncontrollable and often undesirable charge injection process[29,30,25,31] which was used constructively by the induced junction storage correlator is successfully ignored in the implant isolated storage device.

In the following section we present a detailed description of the implant-isolated storage correlator fabrication and operation as well as experimental verification of the existence of induced junction storage regions. Section III consists of an in-depth discussion of charge storage in

the implant-isolated device. An approximation for the effective recombination lifetime of minority carriers is also presented. Experimental results for the implant-isolated storage correlator are given in Section IV followed by conclusions in Section V.

II. THE IMPLANT ISOLATED STRUCTURE

Device Structure

The implant isolated storage correlator, pictured in Fig. 3, consists of an n-type 10 Ω–cm (100)-cut silicon substrate which is ion implanted with phosphorus in a grating pattern at the sample surface. Charge storage, it should be noted, occurs in the non-implanted regions. Subsequent to the grating region implantation, a wet oxidation is performed at 900 °C for 40 minutes. This oxidation, yielding a 1000 Å thick insulating layer, simultaneously passivates the silicon surface and activates the implant. Prior to depositing the 1.7μm ZnO layer by rf sputtering, 1000 Å thick aluminum shorting planes are evaporated on the substrate in the regions below the transducers to enhance the electromechanical coupling. The top aluminum metallization pattern consists of two pairs of single comb transducers[32] and a split gate electrode arranged so as to form a dual track structure[33]. The transducers, used to excite Rayleigh waves, have equal 17.75 μm finger widths and gaps; the center frequency of the transducer response is 128 MHz. The separate comb dual track structure is employed because this technique has been shown to suppress the self convolution caused by reflections from the transducers. By slanting the gate metallization pattern adjacent to the transducers one minimizes the undesirable output observed at the transducers caused by waves launched at the ends of the gate.

Implant Isolation Concept

Insight into operation of the implant isolated storage correlator can best be achieved by understanding the method in which charge is stored in the device. We present a qualitative explanation based on typical n-type MOS capacitance versus voltage characteristics. To first order the ZnO layer can

be modeled as a constant capacitance in series with the constant SiO_2 layer capacitance; the combination can in turn be modeled as a single effective insulating layer. C-V curves for two structurally identical but differently doped MIS-capacitors are displayed in Fig. 4. Note that for both devices, accumulation occurs over the same bias range. However, the onset of inversion occurs for different values of capacitor bias. Suppose the two differently doped devices were side-by-side as part of the same substrate and covered by the same insulator and metal gate. Under this condition a range of gate bias voltages would exist where the higher doped device would be depleted and the lower doped device would be inverted. In the implementation of the implant-isolated storage correlator, higher doped depletion regions are used to isolate the lower doped storage or inversion regions.

To achieve lateral variations in doping density one can employ either ion implantation or diffusion; ion implantation was chosen because it offered advantages in ease of fabrication. Phosphorus was implanted into the unoxidized silicon wafer through a photoresist mask at a concentration level of $8.0 \times 10^{12} / cm^2$ using an implant energy of 25 KeV. The implant concentration varies of course as a function of depth into the semiconductor. An estimate of the doping profile derived from the C-V profiling technique, however, indicates that the semiconductor may be approximately modeled as uniformly doped ($\sim 10^{17} / cm^3$) in the bias ranges of interest. As a result of the ion implantation, a periodic grating pattern of alternating highly doped and lowly doped semiconductor is established beneath the gate of the correlator. The periodicity of the grating corresponds to $5 \mu m$ wide storage regions separated by $5 \mu m$ wide implanted regions. A simple electrical model for the correlator gate appears in Fig. 5, while Fig. 6 shows experimental C-V curves

derived from an unimplanted wafer, a wafer implanted over its entire surface area, and a grating structure wafer. (The rise in the capacitance of the grating structure capacitance near -8.0 volts is caused by lateral effects.) It is apparent from the curves in Fig. 6, that one can select a bias voltage between -1.0 volts and -10.0 volts such that the inverted storage (non-implanted) regions will be electrically isolated from one-another by depletion regions in the implanted areas. This is the desired result as illustrated schematically in Fig. 7. The implant-isolated storage regions, however, in contrast to those formed by charge injection and trapping at the ZnO/SiO_2 interface[26], are established by a repeatable, well-controlled fabrication process and simple selection of the proper operating gate bias.

Verification of Storage Region Isolation

Subsequent to ion implantation, implant activation during thermal oxidation, and deposition of the shorting pad metallization, special gate-pattern test structures were formed directly on the oxidized silicon surface. The test structures were subjected to a post-metallization anneal at 480 °C for five minutes to minimize the SiO_2/Si interface state concentration. Capacitance-versus-time (C-t) transient measurements were then performed on the SiO_2/Si system in order to determine the storage capability of the grating, and to examine the effectiveness of the implant in isolating the storage regions.

The C-t transient results can be readily explained with the aid of Figs. 6 and 8. Figure 8 shows a series of capacitance-versus-time characteristics of the grating region when pulsed from an equilibrium state at $V_G = V_o$ (accumulation) to various voltages (V_A, V_B, etc.) labeled in Fig. 6. Trace A shows the result of pulsing the capacitor from the accumulation reference bias V_o,

to an applied bias which is still in accumulation. As expected, there is no change in capacitance with time. Similarly for Curve B, when both the storage and isolation regions are depleted the t>0 capacitance is time independent, but is lower because of the increased depletion widths of the two regions. Once the device is pulsed such that the non-implanted region beneath the gate is inversion biased (curve C), the sudden pulse causes a deep depletion condition in the non-implanted region with an accompanying finite relaxation time back to equilibrium. The difference in the C-t transient of curves C and D is that a larger negative pulse causes a greater degree of depletion in the implanted region and also a greater deep depletion width in the non-implanted regions. After relaxation, the non-implanted depletion widths remain at their maximum values. However, the total equilibrium capacitance is lower due to the larger depletion width in the implanted region. Once the gate is pulsed from accumulation to a bias tending to invert both the implanted and non-implanted regions, the total capacitance always relaxes to the same minimum value as exemplified by Curves E and F. This is true even though a larger negative pulse deep depletes the capacitors farther and for a longer time. The existence of a biasing range where the device relaxes to a decreasing final capacitance, followed by a biasing range where the final capacitance is always the same independent of bias, is direct verification of the underlying device concept -- implant isolation of the storage regions. The biasing range over which the device relaxes to a decreasing final capacitance corresponds, of course, to the set of biases used in the normal operation of the storage correlator.

III. CHARGE STORAGE

In this section a simple model is presented to describe the information storage process. To gain physical insight, we first examine the response of the storage region inversion layer charge and depletion capacitance to a single narrow pulse. After analyzing the effect of a narrow pulse, the actual rf signal is next treated as a discretized sequence of narrow pulses (details in Appendix).

Charge Storage

Consider the application of a narrow positive pulse to the gate of a device which is biased for normal operation. Under equilibrium inversion conditions, there is a maximum depletion width associated with a given gate voltage. Application of a short duration positive pulse to the gate while it is under equilibrium inversion bias will cause the depletion width to narrow by some amount dependent upon the pulse amplitude and duration; at the same time, minority carrier holes in the inversion layer will be injected into the semiconductor depletion region where some will recombine. Termination of this pulse causes the depletion width to instantaneously assume a new value equal to its equilibrium width plus an increment dependent upon the amount of minority carriers which recombined during the pulse. Herein it is assumed that the recombination rate of injected holes, crucial to information storage, can be modeled by an effective recombination lifetime, τ_R. Moreover, the generation of carriers during the negative going portion of the writing cycle can be neglected because, as is obvious from the lengthy storage times, the return to equilibrium is very slow compared to the writing recombination rate. Surface states, traps in the semiconductor and ZnO, and charges in the oxides will also be neglected because they complicate the

analysis without offering any insight into the writing process.

As discussed in Section II, proper operation of this device is dependent upon the selection of an appropriate operating point gate bias. Assuming that a bias of V_G has been applied to the gate, one can, using the δ-depletion approximation, calculate the inversion layer charge at the silicon surface. Because the ZnO layer is only semi-insulating, the d.c. charge applied to the gate is readily injected into the ZnO film and is subsequently stored in traps adjacent to the ZnO/SiO$_2$ interface, i.e., under steady-state conditions a virtual gate is formed at the ZnO/SiO$_2$ interface[31]. The ZnO layer, therefore, can be neglected when calculating the equilibrium minority carrier inversion charge density whose magnitude is given by

$$Q_{inv_{eq}} = C_o \left[V_G - \frac{2kT}{q} U_F - \frac{qN_D}{C_o} \sqrt{\frac{4\kappa_s \varepsilon_o}{qN_D} \frac{kT}{q} |U_F|} \right] \quad . \tag{1}$$

where C_o is the capacitance (per unit area) of the SiO$_2$ layer, N_D is the background doping level of the n-type silicon substrate, and U_F is the substrate doping parameter. The dielectric constant of the silicon is represented by κ_s, the temperature by T, ε_o is the permittivity of free space, and k is Boltzmann's constant. The constant U_F is given by

$$U_F = - \ln\left(\frac{N_D}{n_i}\right) \quad . \tag{2}$$

where n_i is the intrinsic carrier concentration.

Due to the localization of injected charge at the ZnO/SiO$_2$ interface, the equilibrium inversion layer charge is independent of the ZnO layer capacitance. However, this is not true of the inversion layer charge density when there are rapid changes in the gate bias. For rf signals in the frequency range of interest, voltage changes are too fast for the gate-injected electrons

to follow the applied signal. Hence the capacitance of the ZnO layer must be included in any calculation of the redistributed surface charge. The condition just described can be visualized more easily with the aid of Fig. 9. In this figure, the solid curve represents a normal C-V characteristic for an n-type semiconductor; V_G is the bias point. In a normal MOS capacitor one would have to pulse the gate to some bias greater than V_T to move out of inversion and into depletion. In the case of a correlator with an injecting ZnO film, however, the gate must be pulsed to $V_{T_{oft}}$ (on the dashed curve) to be at the edge of inversion. For comparison to the redistributed charge it is therefore more convenient to rewrite the equilibrium inversion layer charge density (Eq. 1) for a given gate bias V_G in terms of $V_{T_{eff}}$ and C_I (the series combination of the ZnO and SiO$_2$ capacitances). The resulting expression for Q_{seq} is given by

$$Q_{seq} = C_I \left[V_G + V_{T_{eff}} - \frac{2kT}{q} U_F - \frac{qN_D}{C_I} \sqrt{\frac{4\kappa_s \varepsilon_o}{qN_D} \frac{kT}{q} |U_F|} \right] \qquad (3)$$

where

$$C_I = \frac{C_{SiO_2} C_{ZnO}}{C_{SiO_2} + C_{ZnO}} \qquad (4)$$

If the applied pulse were of amplitude V_A, repeated applications of such a pulse within an interval that is short compared to the device storage time (~ 1 sec) eventually leads to a "steady-state" deep depletion condition beneath the gate where the new inversion layer surface charge density, Q_A, saturates at

$$Q_A = C_I \left[V_G - V_A + V_{T_{eff}} - \frac{2kT}{q} U_F - \frac{qN_D}{C_I} \sqrt{\frac{4\kappa_s \varepsilon_o}{qN_D} \frac{kT}{q} |U_F|} \right] \qquad (5)$$

The maximum charge storage in the implant-isolated storage correlator for a given V_A is therefore

$$\Delta Q = Q_{seq} - Q_A = C_I V_A \qquad (6)$$

Assuming an effective recombination lifetime, the application of a dc pulse of amplitude V_A and arbitrary duration t_p changes the inversion layer charge by an amount

$$\Delta Q_s = C_I V_A (1 - e^{-t_p/\tau_R}) \qquad (7)$$

The expression for the inversion layer surface charge as a function of gate bias, applied pulse magnitude, and applied pulse duration is given by

$$Q_s(V_G, V_A, t_p) = Q_{seq} - C_I V_A (1 - e^{-t_p/\tau_R}) \qquad (8)$$

If one were to pulse the device again immediately after the application of the first pulse, the starting inversion layer minority carrier density would be $Q_s(V_G, V_A, t_p)$ instead of Q_{seq}.

As mentioned above, the change in surface charge caused by recombination during a positive pulse of duration t_p results in an increase in the depletion width of the storage regions; the new depletion width is given by

$$W(V_G, V_A, t_p) = \frac{\kappa_s \varepsilon_0}{C_o} \left[-1 + \left(1 + \frac{V_G - \dfrac{Q_s(V_G, V_A, t_p)}{C_o}}{V_\Delta} \right)^{\!\!\frac{1}{2}} \right] \qquad (9)$$

where

$$V_\Delta = \frac{\kappa_s \varepsilon_0 q N_D}{2 C_o^2} \qquad (10)$$

The modified depletion width corresponds to a decreased capacitance given by

$$C(V_G, V_A, t_p) = \frac{C_I}{1 + \dfrac{C_I}{C_o}\left[-1 + \left(1 + \dfrac{V_G - \dfrac{Q_s(V_G, V_A, t_p)}{C_o}}{V_\Delta} \right)^{\!\!\frac{1}{2}}\right]} \qquad (11)$$

Effective Recombination Lifetime

An experiment was performed to obtain the effective recombination life-time, τ_R. Determination of τ_R was accomplished by monitoring the variation in correlation output with the number of identical writing sequences between each identical readout step. Each write sequence consisted of a 1.0 μs gate reference signal written by a 400 ns rf writing signal which was applied to one transducer (gate-acoustic writing mode). Results of this variable-write correlation experiment are shown in Fig. 10 which is a semilog plot of one minus the normalized correlation output versus effective write time. Effective write time is simply the number of writes performed between each readout multiplied by the write signal duration (400 ns). (It should also be noted that in this experiment the time between readouts was several seconds to ensure sufficient decay of the stored signal before initiating a new write sequence.) The value of τ_R was determined to be 6.3 μs by fitting the eq. (7) dependence to the measured correlation output.

IV. OPERATIONAL CHARACTERISTICS

In this section we present experimental results for the correlation of two 1.0μs rf bursts in order to examine correlator storage time, dynamic range and efficiency. All correlation measurements were performed using the rf gate-acoustic writing mode and the gate-to-acoustic reading mode. It should be pointed out that the implant-isolated storage correlator presented in this paper is bias stable; results of all correlation measurements are totally repeatable at any time without any special precautions, irrespective of the previous gate bias.

A key feature of the implant isolated correlator device is the time the device is capable of storing a reference signal. Figure 11 displays the correlation output versus storage time, the data points fall along the dashed curve which corresponds to a 3 dB storage time of 0.56 seconds. Although this is certainly a long storage time compared to other previous MZOS correlator configurations, with advanced fabrication procedures it is not unreasonable to expect storage times of at least several seconds.

A plot of normalized correlation output versus gate bias is shown in Fig. 12 for three different values of read-write power level combinations. It is seen that for gate biases less than a certain value, the correlation output always remains within 85% of its maximum. This indicates a very wide bias range over which one may operate the device without significant degradation of the output signal. Based on theoretical considerations, one might expect that once the d.c. gate bias was sufficiently large to invert not only the storge regions, but also the ion implanted separation (and lateral) regions, then the lateral flow of inversion layer minority carriers from implanted regions surrounding the storage areas would eliminate the stored signal. The

experimental result presented, however, indicates that the implanted region is of insufficient area to supply the signal eliminating flow of minority carriers. The top surface of the device after sawing and mounting extends approximately one millimeter to either side of the one millimeter wide gate. This area is subject to lateral effects and should contribute to the overall relaxation, but it is apparently too small to degrade the output significantly.

An rf writing signal of 140 nanoseconds (18 cycles) was found to produce the highest correlation output, and this writing pulse duration was used when performing the correlation measurements shown in Fig. 13. Figure 13a shows the correlation output versus the reference signal amplitude and the result is linear over a 25 dB range in correlator output power. The correlation output versus read pulse power can be seen in Figure 13b, here again the dynamic range of the device is approximately 25 dB. In all measurements the correlation efficiency is between -100 and -110 dBm. The efficiency and dynamic range of this device are lower than expected. ZnO film quality during this particular sputter produced a delay line insertion loss some 14 dB more than in previous devices with the same dimensions. (The same was true for non-implanted test structures.) A better piezoelectric film should upgrade both figures of merit into the range of previously reported monlithic memory correlators

IV. CONCLUSIONS

A monolithic MZOS surface acoustic wave memory correlator has been presented which utilizes ion implantation to confine induced junction storage regions. The storage time capability of the device before fabrication is completed has been demonstrated by means of a pulsed capacitance-versus-time experiment. A simple model of the writing process was detailed which allows one to determine an effective minority carrier lifetime for the inversion layer charge. It has been demonstrated that 3 dB storage times in excess of 0.5 seconds are achievable with the promise of signal storage up to several seconds. Finally, this device exhibits bias stability, making the implant isolated storage correlator an attractive device for use as an on-chip circuit element.

Acknowledgements

APPENDIX

For a single pulse applied to a storage region one has, after a rectangular pulse of amplitude V_1 and duration Δt_1, a modified surface charge density of Q_1 given by

$$Q_1 = Q_{seq} - C_1 V_1 (1 - e^{-\Delta t_1 / \tau_R}) \quad . \tag{A.1}$$

If one applies another pulse of amplitude V_2 and duration Δt_2 at some instant immediately after turning off pulse V_1, then the surface charge density is given by

$$Q_2 = Q_{seq} - C_1 V_2 + \left[Q_1 - (Q_{seq} - C_1 V_2) \right] e^{-\Delta t_2 / \tau_R} \tag{A.2}$$

$$= Q_{seq} - C_1 V_2 (1 - e^{-\Delta t_2 / \tau_R}) - C_1 V_1 e^{-\Delta t_2 / \tau_R} (1 - e^{-\Delta t_1 / \tau_R}) \quad .$$

Similarly, with the application of numerous narrow pulses of amplitudes V_i, one can replicate any time varying signal. If one discretizes the desired signal into uniform increments of duration Δt, one can determine the surface charge density for the application of a signal $N\Delta t$ long by

$$Q_N = Q_{seq} - C_1 (1 - e^{-\Delta t / \tau_R}) \left[\sum_{i=1}^{N} V_i e^{-(n-i)\Delta t / \tau_R} \right] \quad . \tag{A.3}$$

References

1. L. G. Pearce, R. L. Gunshor, and R. F. Pierret, "Aluminum Nitride on Silicon Surface Acoustic Wave Devices," *Appl. Phys. Lett.*, vol. 39, no. 11, pp. 878-879, December 1, 1981.

2. K. Tsubouchi and N. Mikoshiba, "Zero Temperature Coefficient SAW Delay Line on AlN Epitaxial Films," *IEEE Ultrasonics Symposium Proceedings*, pp. 299-310, 1983.

3. C. W. Lee and R. L. Gunshor, "Nonlinear Interaction of Acoustic Surface Waves from Coupling to Charge Carriers," *J. Appl. Phys.*, vol. 44, no. 11, pp. 4807-4812, November 1973.

4. W. C. Wang, "Convolution of Surface Waves in a Structure of Semiconductor on LiNbO$_3$," *Appl. Phys. Lett.*, vol. 20, no. 10, pp. 389-392, May 15, 1972.

5. P. Das, M. N. Araghi, and W. C. Wang, "Convolution of Signals Using Surface Wave Delay Line," *Appl. Phys. Lett.*, vol. 21, no. 4, pp. 152-154, August, 1972.

6. M. Yamanishi, T. Kawamura, and Y. Nakayama, "Acoustic Surface Wave Convolver Using Nonlinear Interaction in a Coupled PZT-Si System," *Appl. Phys. Lett.*, vol. 21, no. 4, pp. 146-148, August, 1972.

7. G. S. Kino, W. R. Shreve, and H. R. Gautier, "Parametric Interactions of Rayleigh Waves," *IEEE Ultrasonics Symposium Proceedings*, pp. 285-287, 1972.

8. R. L. Gunshor, "The Interaction Between Semiconductors and Acoustic Surface Waves--A Review," *Solid-State Electron.*, vol. 18, pp. 1089-1093, 1975.

9. R. W. Ralston, J. H. Cafarella, S. A. Reible, and E. Stern, "Improved Acoustoelectric Schottky-Diode/LiNbO$_3$ Memory Correlator," *IEEE Ultrasonics Symposium Proceedings*, pp. 472-477, 1977.

10. T. Shiosaki, T. Yamamoto, and A. Kawabata, "Higher Order Mode Rayleigh Waves Propagating on ZnO/Substrate Structures," *IEEE Ultrasonics Symposium Proceedings*, pp. 814-818, 1977.

11. J. K. Elliott, R. L. Gunshor, R. F. Pierret, and A. R. Day, "A Wideband SAW Convolver Utilizing Sezawa Waves in the Metal–ZnO–SiO$_2$–Si Configuration," *Appl. Phys. Lett.*, vol. 32, no. 9, pp. 515-516, May 1, 1978.

12. F. C. Lo, R. L. Gunshor, and R. F. Pierret, "Monolithic (ZnO) Sezawa-mode P-N Diode-Array Memory Correlator," *Appl. Phys. Lett.*, vol. 34, no. 11, pp. 725-726, June 1, 1979.

13. S. Minigawa, T. Okamoto, R. Asai, and Y. Sato, "Efficient Monolithic ZnO/Si Sezawa Wave Convolver," *IEEE Ultrasonics Symposium Proceedings*, 1982.

14. J. E. Bowers, B. T. Khuri-Yakub, and G. S. Kino, "Monolithic Sezawa Wave Storage Correlators and Convolvers," *IEEE Ultrasonics Symposium Proceedings*, pp. 98-103, 1980.

15. R. L. Gunshor and C. W. Lee, "Generation of a Surface Acoustic Wave Correlation Echo from Coupling to Charge Carriers," *Appl. Phys. Lett.*, vol. 21, no. 1, pp. 11-12, July, 1972.

16. M. Luukkala and G. S. Kino, "Convolution and Time Inversion Using Parametric Interactions of Acoustic Surface Waves," *Appl. Phys. Lett.*, vol. 18, no. 9, pp. 393-394, May 1, 1971.

17. A. Bers and J. H. Cafarella, "Surface State Memory in Surface Acous-

toelectric Correlator," *Appl. Phys Lett*, vol. 25, no. 3, pp. 133-135, August 1, 1974.

18. H. Hayakawa and G. S. Kino, "Storage of Acoustic Signals in Surface States in Silicon," *Appl Phys. Lett*, vol. 25, pp. 178-180, 1974.

19. C. Maerfeld, Ph. Defranould, and P. Tournois, "Acoustic Storage and Processing Device Using P-N Diodes," *Appl. Phys. Lett*, vol 27, no. 11, pp. 577-578, December 1, 1975.

20. H. C. Tuan, B. T. Khuri-yakub, and G. S. Kino, "A New Zinc-oxide-on-Silicon Monolithic Storage Correlator," *IEEE Ultrasonics Symposium Proceedings*, pp. 496-499, 1977.

21. P. G. Borden, R. Joly, and G. S. Kino, "Correlation With the Storage Convolver," *IEEE Ultrasonics Symposium Proceedings*, pp. 348-351, 1976.

22. F. C. Lo, R. L. Gunshor, R. F. Pierret, and J. K. Elliott, "Separation of Storage Effects in Monolithic P-N Diode Correlators," *Appl. Phys. Lett.*, vol. 33, no. 11, pp. 903-905, December 1, 1978.

23. K. A. Ingebrigtsen, R. A. Cohen, and R. W. Mountain, "A Schottky-Diode Acoustic Memory and Correlator," *Appl Phys. Lett.*, vol. 26, no. 11, pp. 596-598, June 1, 1975.

24. K. A. Ingebrigtsen, "The Schottky Diode Acoustoelectric Memory and Correlator-A Novel Programmable Signal Processor," *Proc. IEEE*, vol. 64, no. 5, pp. 764-769, May 1976.

25. W. C. Wang, "Physical Processes of SAW Schottky-Diode Memory Correlaotor," *Electron. Lett.*, vol 12, pp 105-106, 1976

26. K. C. K. Weng, R. L. Gunshor, and R. F. Pierret, "Induced Junction Monolithic Zinc Oxide-on-Silicon Storage Correlator," *Appl Phys Lett.*, vol. 40,

pp. 71-73, 1982.

27. J. K. Elliott, R. L. Gunshor, R. F. Pierret, and K. L. Davis, "Characteristics of Zinc Oxide-Silicon Surface Wave Convolvers for Optical Imaging and Memory," *IEEE Ultrasonics Symposium Proceedings*, pp. 141-143, 1975.

28. K. L. Davis, "Properties of the MZOS Surface Wave Convolver Configuration," *IEEE Trans. Electron Devices*, vol. 23, no. 6, pp. 554-559, June 1976.

29. L. A. Coldren, "Effect of Bias Field in a Zinc-Oxide-on-Silicon Acoustic Convolver," *Appl. Phys. Lett.*, vol. 25, no. 9, pp. 473-475, November 1, 1974.

30. J. K. Elliott, R. L. Gunshor, R. F. Pierret, and K. L. Davis, "Zinc Oxide-Silicon Monolithic Acoustic Surface Wave Optical Image Scanner," *Appl. Phys. Lett.*, vol. 27, no. 4, pp. 179-182, August 15, 1975.

31. R. F. Pierret, R. L. Gunshor, and M. E. Cornell, "Charge Injection in Metal–ZnO–SiO$_2$–Si Structures," *J. Appl. Phys.*, vol. 50, no. 12, pp. 8112-8124, December 1979.

32. M. R. Melloch, R. L. Gunshor, and R. F. Pierret, "Single Phase and Balanced Separate Comb Transducer Configurations in a ZnO/Si SAW Structure," *IEEE Trans. on Sonics and Ultrasonics*, vol. 28, 1982.

33. I. Yao, "High Performance Elastic Convolver with Parabolic Horns," *IEEE Ultrasonics Symposium Proceedings*, 1980.

FIGURE CAPTIONS

Fig. 1   Schematic of a typical monolithic SAW correlator.

Fig. 2   Correlation and convolution using a storage correlator.

Fig. 3   Schematic diagram of an implant-isolated storage correlator. (a) Top view of dual gate structure and single comb transducers. (b) Ion implantation pattern. (c) Side view of completed device

Fig. 4   Normalized C-V curves for typical MOS capacitors
(A) highly doped (1.25×10^{17} / cm^3) n-type Si
(B) moderately doped (5.0×10^{14} / cm^3) n-type Si.

Fig. 5   Electrical model for the gate of the implant-isolated storage correlator. The implanted and non-implanted regions are denoted by C_{im} and C_N respectively. R_{Si} is the bulk silicon resistance and C_I is the combined oxide capacitance.

Fig. 6   Experimentally determined C-V characteristics derived from a (A) totally implanted (B) combined (grating) (C) non-implanted wafer (V_A, V_B, etc. refer to the curves in Fig. 8)

Fig. 7   Schematic of charge storage regions (induced junctions) established beneath the gate of the correlator. Plus signs denote inversion layer charge.

Fig. 8   Capacitance versus time (C-t transient) results for applied pulses described in the text.

Fig. 9   (a) Depletion width of a single storage region in inversion surrounded by depleted highly doped regions. (b) Energy band diagram drawn along the SiO_2/ Si surface.

Fig. 10   C-V characteristics of a typical MIS capacitor (solid curve) and an MZOS capacitor exhibiting charge injection into the ZnO.

Fig. 11   Correlation output versus effective write time displaying exponential dependence. Solid curve corresponds to an effective minority carrier lifetime of $\tau_R = 6.3 \ \mu s$.

2

\

Fig. 1

- 32 -

$R(t) \ast\ast S(t)$

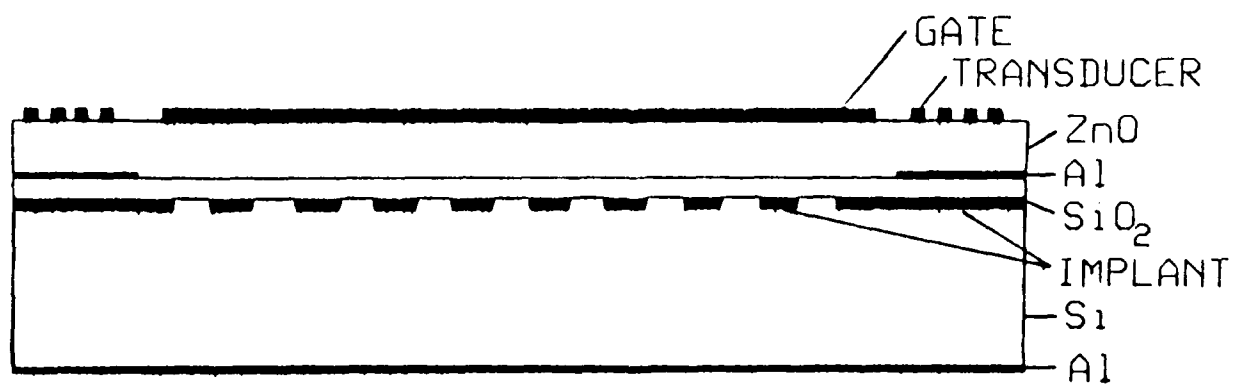$R(t)e^{j\omega t}$

$S(x)e^{-jkx}$

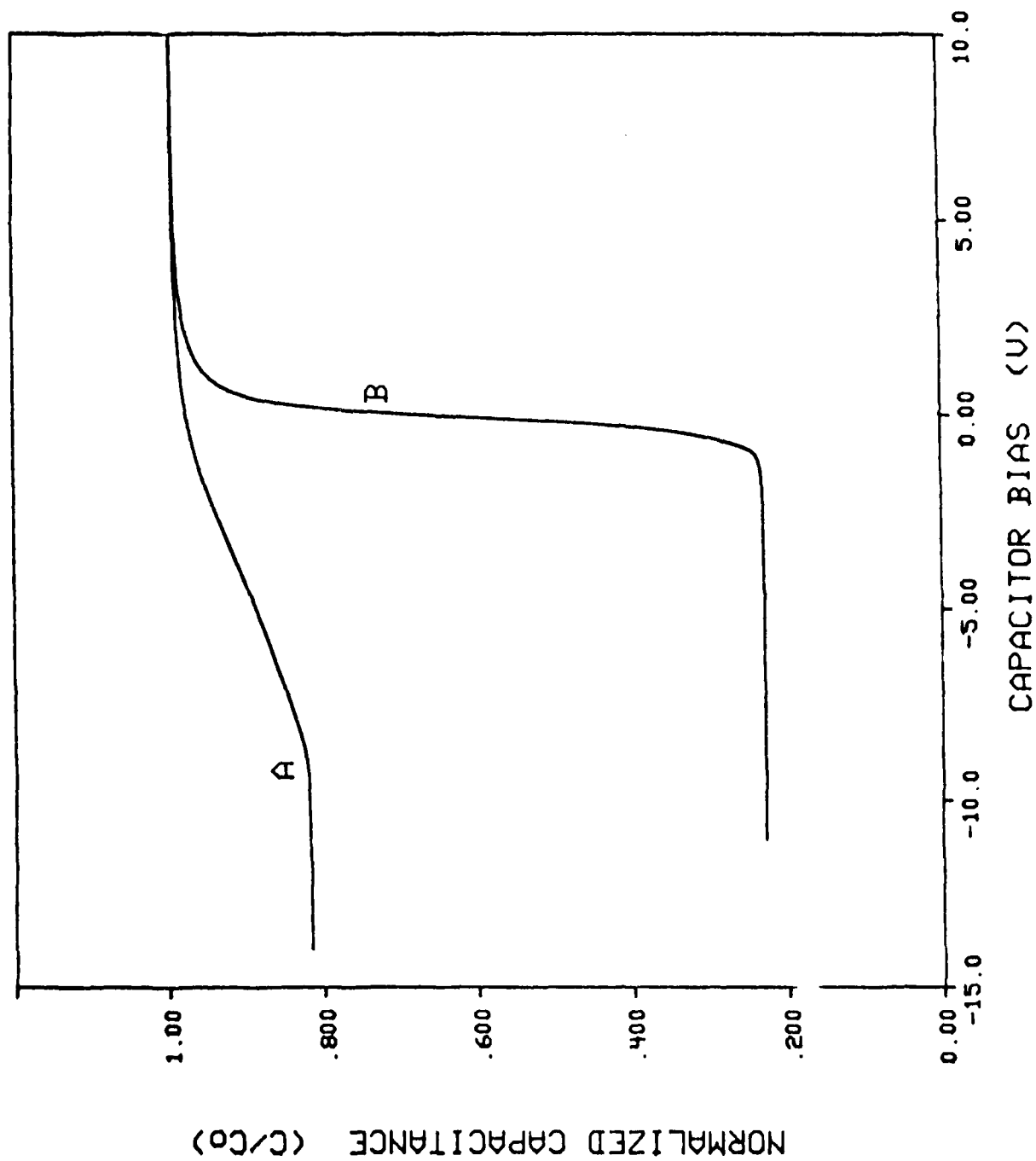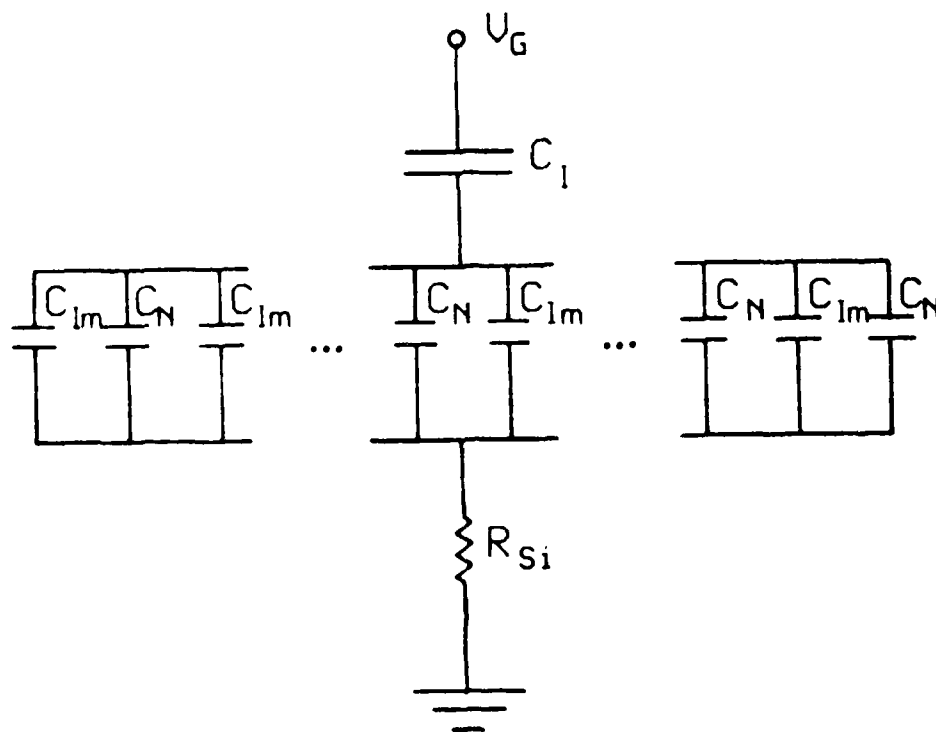$R(t) \ast S(t)$
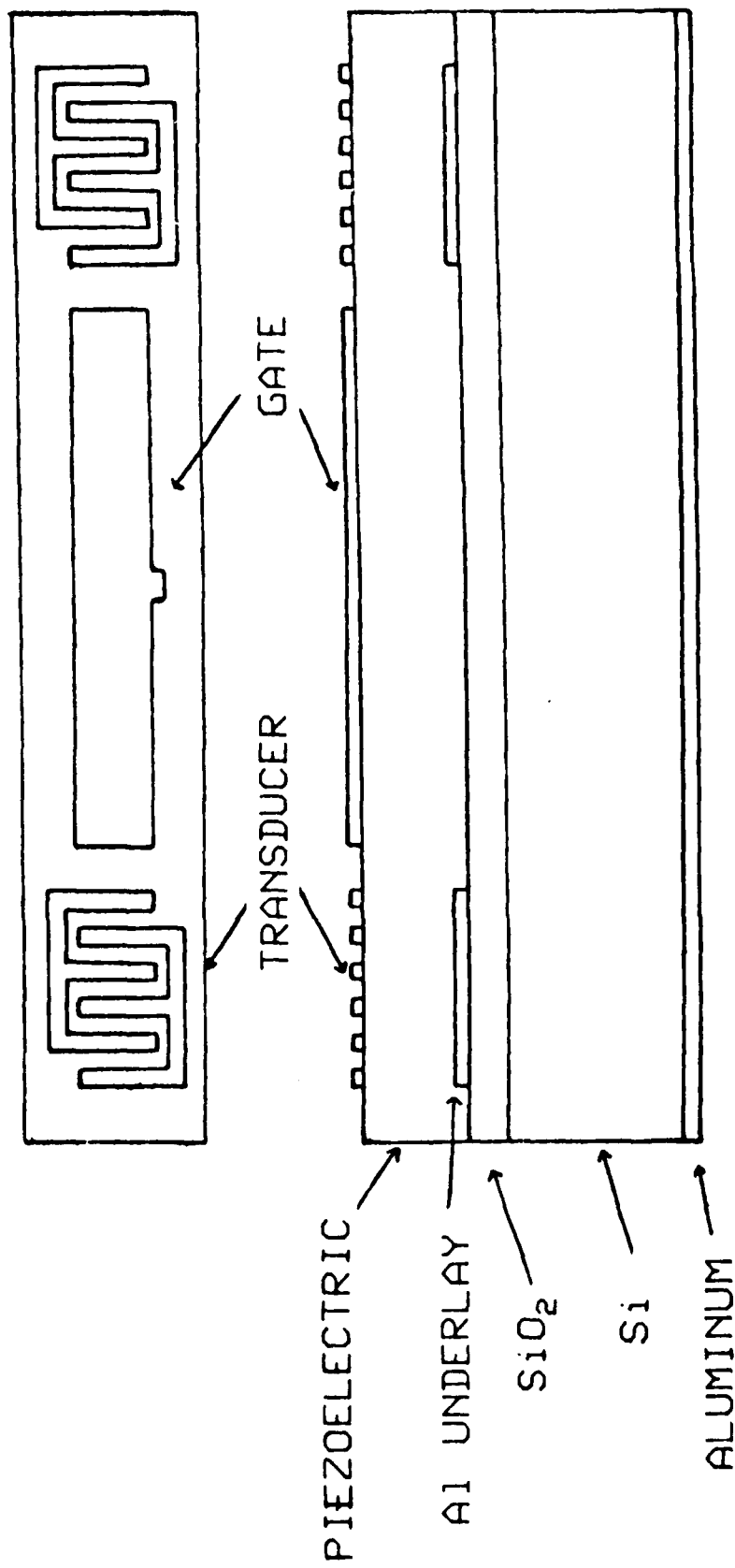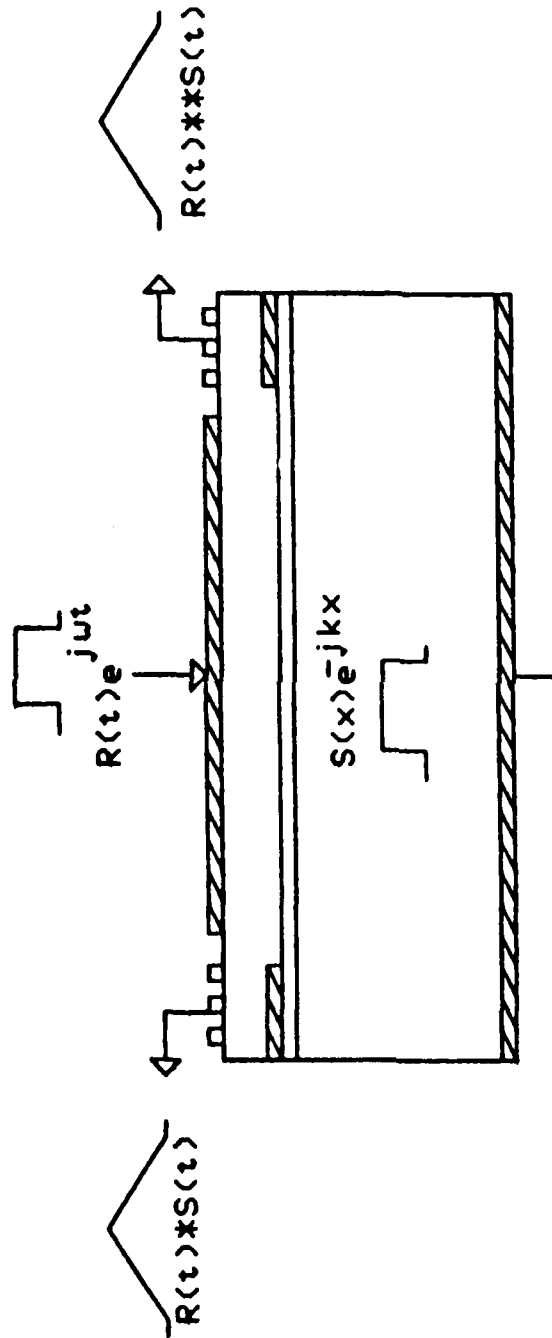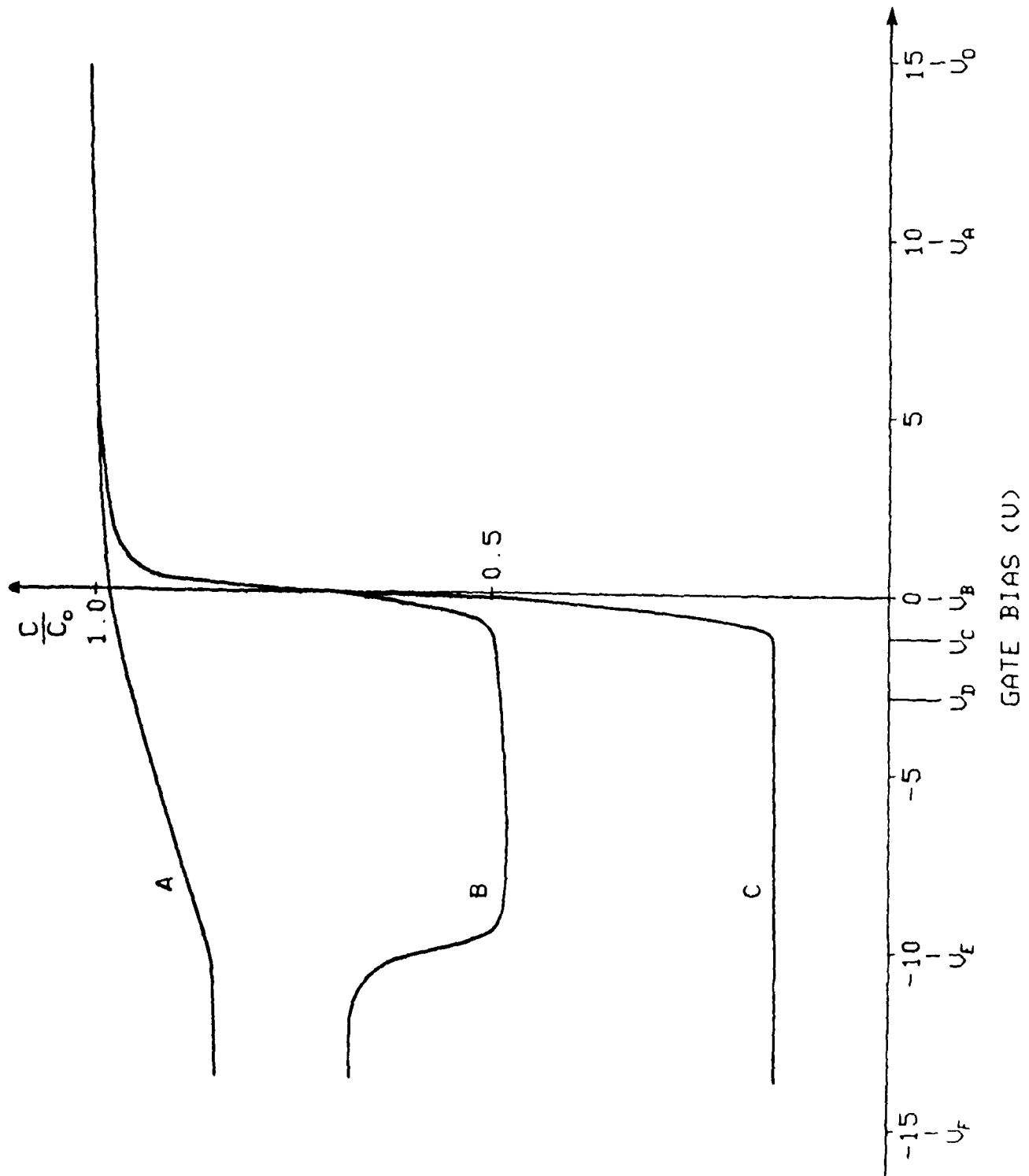
* : CONVOLUTION

** : CORRELATION

Fig. 2

(a)

(b)

(c)

- 34 -

Fig. 4

$$V_G$$

$$C_1$$

$$C_{1m} \quad C_N \quad C_{1m} \quad \cdots \quad C_N \quad C_{1m} \quad \cdots \quad C_N \quad C_{1m} \quad C_N$$
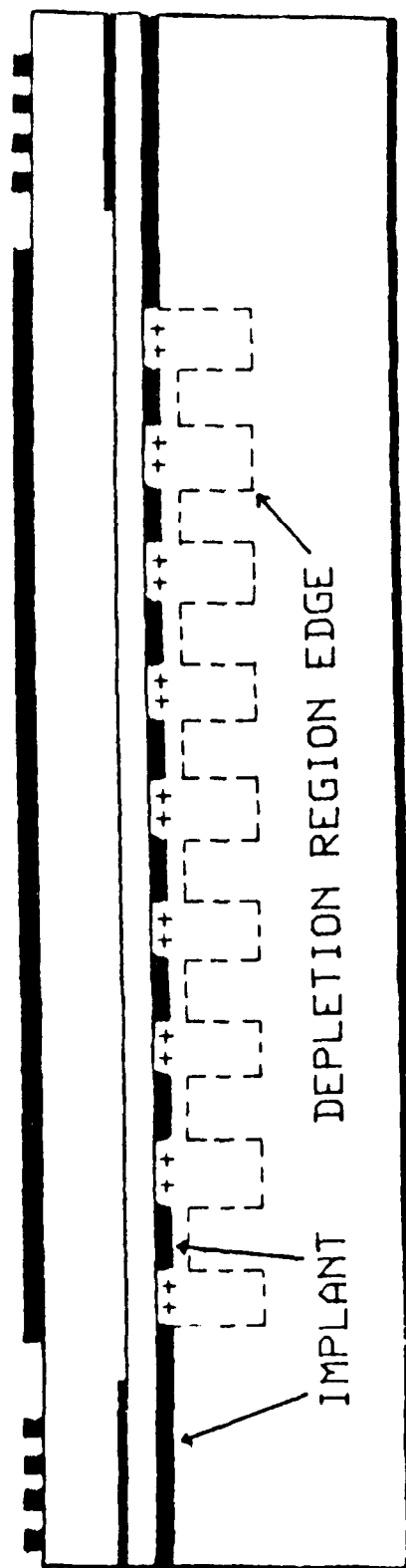
$$R_{Si}$$

F. 5

Fig. 4

IMPLANT

DEPLETION REGION EDGE
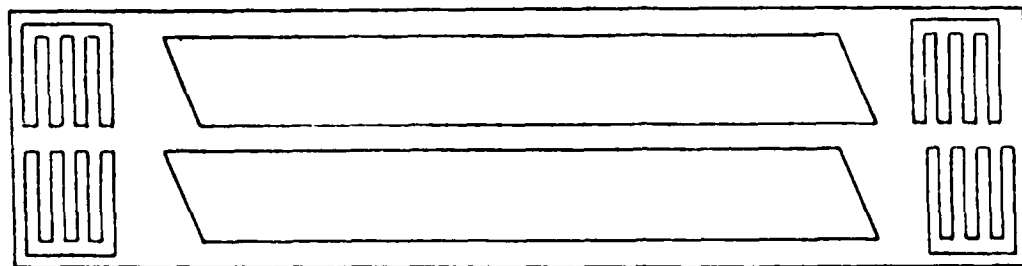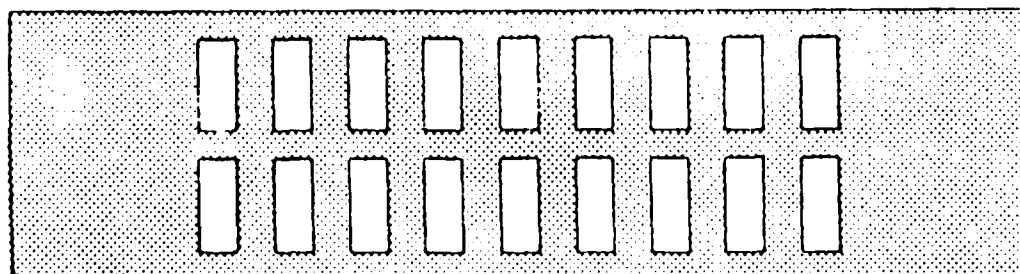
Fig 7

Fig. 8

Fig.9

Fig. 10

Fig. 11
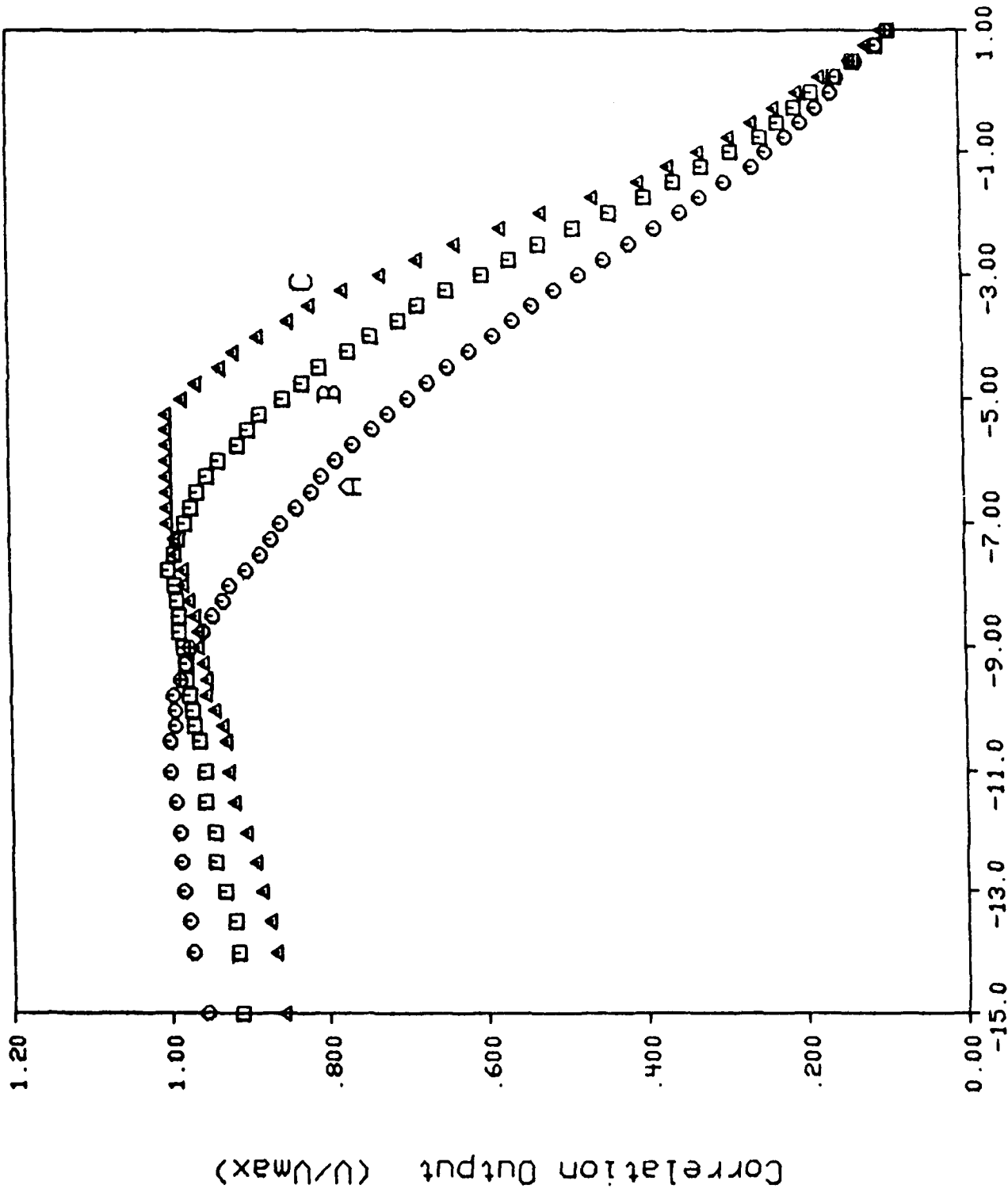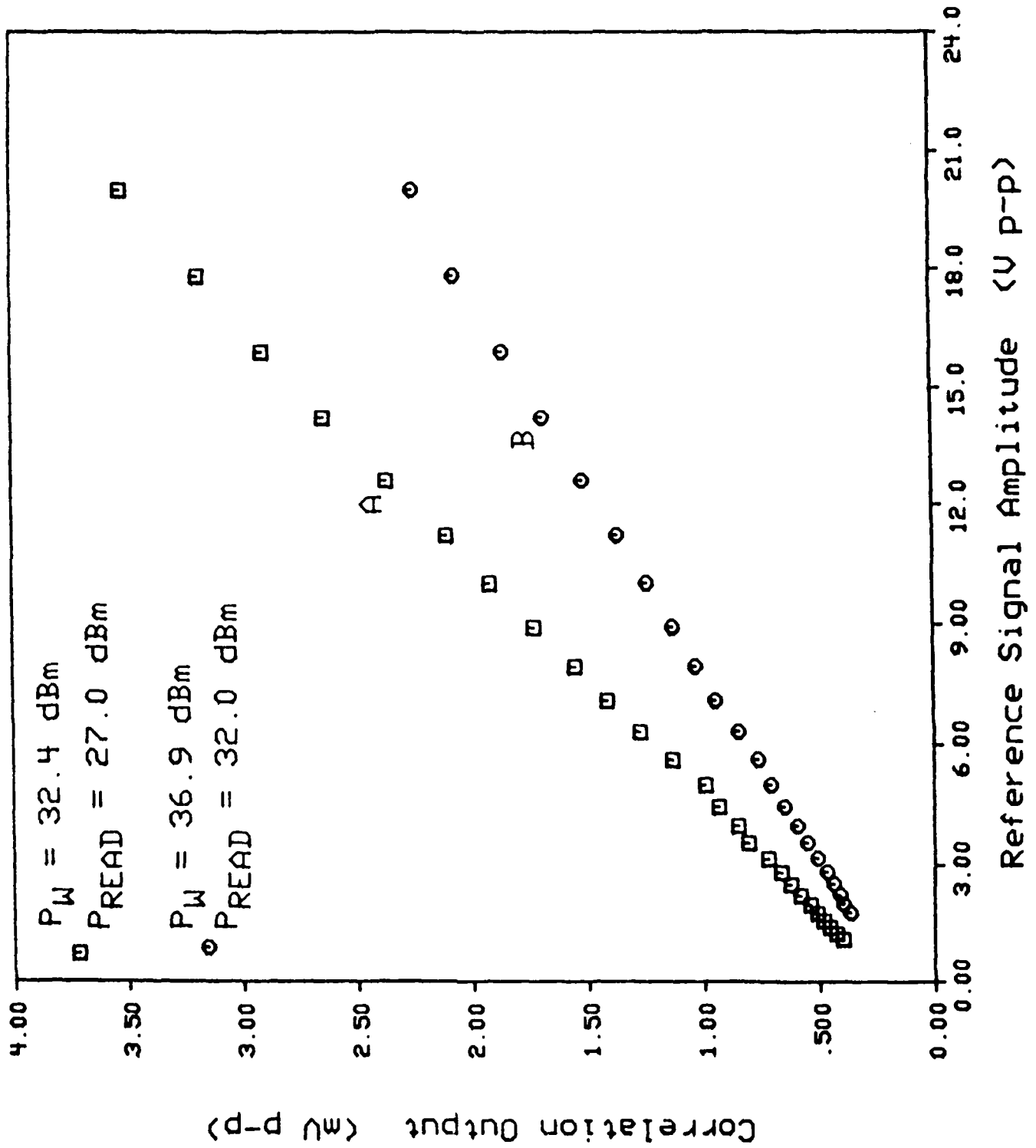
Fig. 12

Axis labels: Correlation Output (U/Umax), Gate Bias (U), curves labeled A, B, C

Fig. 13a

$P_W = 32.4$ dBm
$\boxdot\; P_{READ} = 27.0$ dBm

$P_W = 36.9$ dBm
$\odot\; P_{READ} = 32.0$ dBm

Correlation Output (mV p-p)

Reference Signal Amplitude (V p-p)

Fig 136

APPENDIX B
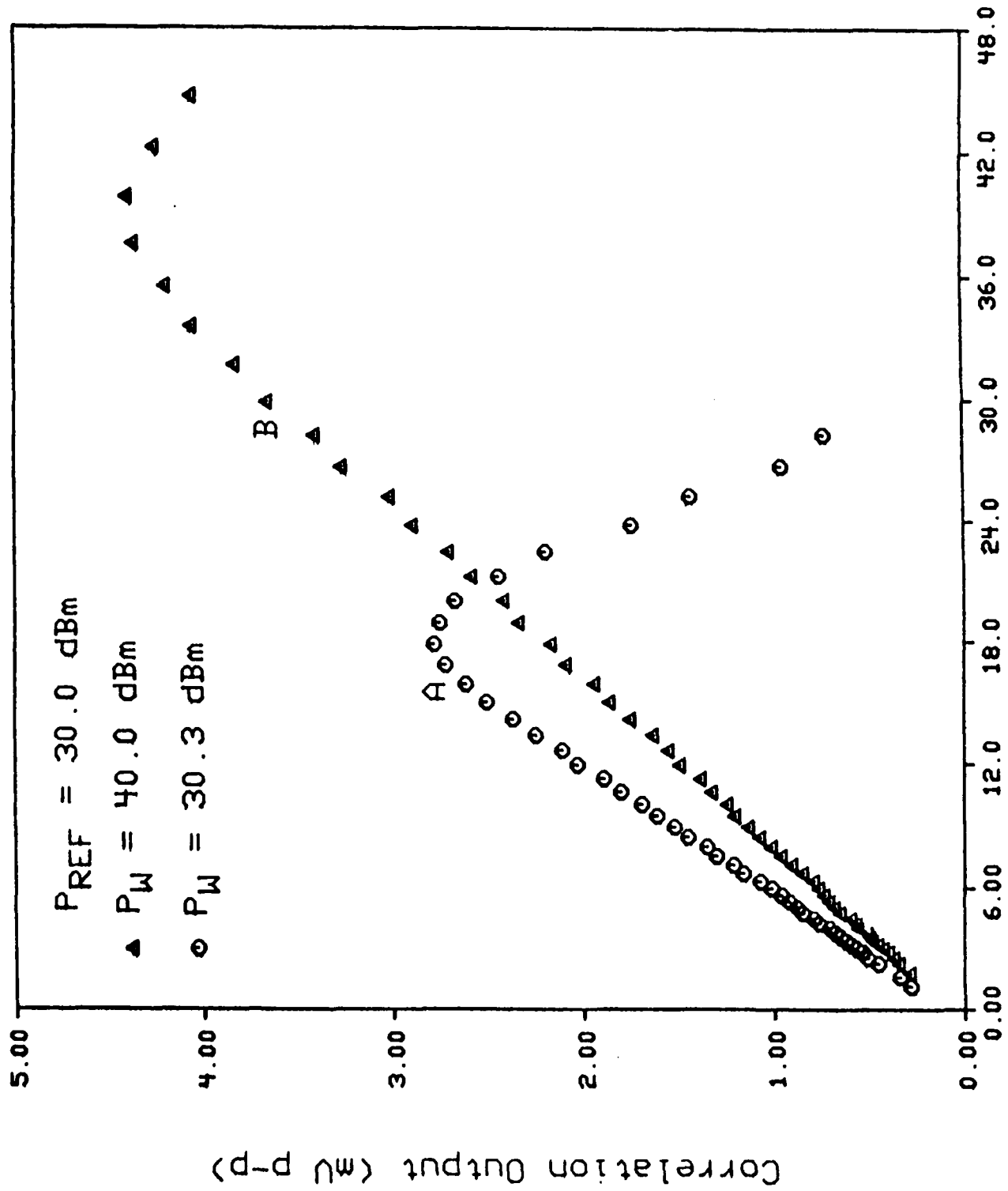
REFLECTION AND MODE CONVERSION OF SURFACE ACOUSTIC WAVES
IN LAYERED MEDIA

Supriyo Datta
School of Electrical Engineering
Purdue University
West Lafayette, IN 47907

Abstract

We present a simply theory for calculating the first-order mechanical reflection coefficient of surface acoustic waves due to a strip overlay. The theory is applicable to both single crystal and layered substrates. The substrate is characterized by the particle velocities at the surface due to an unperturbed surface wave carrying a given amount of power per unit beamwidth while the strip material is characterized by its mass-density and elastic constants. With a straightforward extension, the theory can be used even when the incident and reflected waves belong to different modes. The theory is developed by analogy with transmission lines (rigorous derivations have been presented elsewhere), and the predictions are compared to available experimental data.

I. Introduction

The basic problem we wish to address is as follows: A surface wave of amplitude A^+ propagating on a substrate (which may be a single material like Lithium Niobate or a layered medium like Zinc Oxide-on-Silicon) meets a discontinuity at the surface (Fig. 1). The discon-
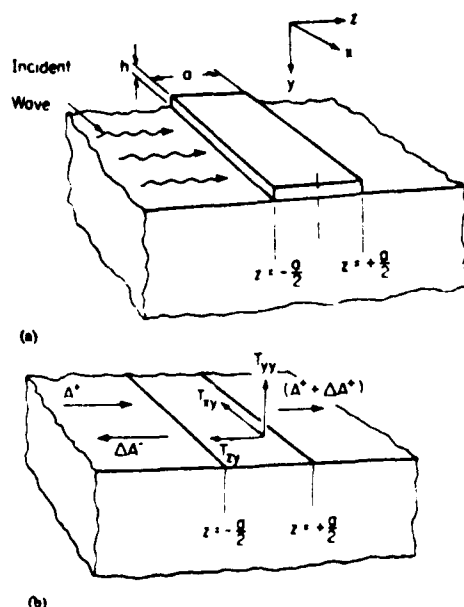

(a)

(b)

Fig. 1: (a) Surface wave incident on thin-strip overlay
(b) Generation of a reflected wave by stresses induced at strip-substrate interface.

tinuity may be due to an electrode or due to grooves etched on the surface. We wish to know the amplitude of the reflected wave, ΔA^-. Normally both the incident and the reflected wave are Rayleigh waves; however, in layered media we also have the possibility of one of the waves being a Rayleigh wave and the other a Sezawa wave. This problem is in general a very difficult one; however, if the height h of the discontinuity is small compared to a wavelength $(h/\lambda < .01 - .02)$ the problem can be treated in a fairly simple manner using perturbation theory. The condition of small h/λ is usually satisfied in practical devices; large values of h/λ result in significant bulk mode conversion which is unacceptable for device operation.

The method used is basically the same as that described by Auld[1] in his book with a modification to incorporate edge effects.[2,3] A rigorous derivation of this theory based on the normal mode analysis is described in detail in Refs. 3 and 4. In this paper we will not develop the theory rigorously; instead we will develop it by analogy with a simple transmission line pointing out the similarities and differences. The theoretical predictions are compared with experimental results for different substrate and electrode combinations. The substrate is characterized by the particle velocities at the surface due to an unperturbed surface wave carrying a given amount of power per unit beamwidth, while the strip material is characterized by its mass-density and elastic constants. The same formulation is used for both single crystal and layered substrates. With a straightforward extension, the theory can be used when the incident and reflected waves belong to different modes (such as Rayleigh and Sezawa).

II. Transmission Line Analogy

The simplest analogy to our present problem is that of reflections in a transmission line (Fig. 2). The discontinuity is represented by a region whose characteristic impedance $Z_0 + \Delta Z$ is slightly different from the usual impedance Z_0, with $\Delta Z/Z_0 \ll 1$. There is a reflection of $+\Delta Z/2Z_0$ at the leading edge and $-\Delta Z/2Z_0$ at the trailing edge. If we use the center of the discontinuity as our reference plane, the voltage reflection coefficient is given by

$$\frac{\Delta V^-}{V^+} = \frac{\Delta Z}{2Z_0}\left(e^{j\theta} - e^{-j\theta}\right) = j\frac{\Delta Z}{Z_0}\sin\theta \qquad (1)$$

where $\theta = ka = 2\pi a/\lambda$. Eq. (1) gives us the reflection coefficient if we know $\Delta Z/Z_0$; the main problem in our case, of course, is to figure out the right $\Delta Z/Z_0$ for a given electrode-substrate combination. The same problem may be viewed in a somewhat different manner which
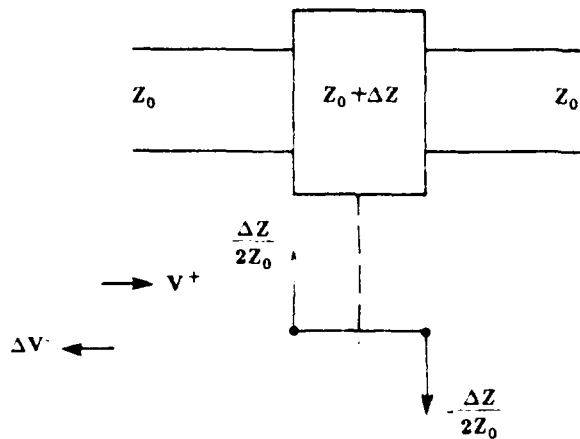
Fig. 2 Reflection from a mismatched section in a transmission line.

gives the same results for transmission lines but generalizes more readily to our problem. The change in characteristic impedance ΔZ can be due to a change ΔL in the inductance L_0 per unit length and/or due to a change ΔC in the capacitance C_0 per unit length; let us assume that $\Delta L = 0$, so that

$$\frac{\Delta Z}{Z_0} = -\frac{\Delta C}{2C_0} \quad \text{since } Z_0 = \sqrt{\frac{L_0}{C_0}} \quad (2)$$

The incident wave V^+ induces a current $-j\omega \Delta C V^+$ when it meets the extra capacitance ΔC per unit length (Fig. 3). This current is given by

$$I(z)\,dz = -j\omega\Delta C\,dz\,V^+ \quad (3)$$

The induced current now acts as a source that generates reflected waves.

$$dV = \frac{Z_0}{2} I(z)dz \quad (4)$$

Using Equations (2), (3) and the relation $k = \omega C_0 Z_0$ we get

$$\frac{dV}{V^+} = j(2k)\cdot\frac{\Delta Z}{2Z_0}\,dz \quad (5)$$

The total reflection is obtained by integrating Eq. (5) after introducing the phase factor e^{+j2kz} so as to shift all the reflections to a common reference plane.
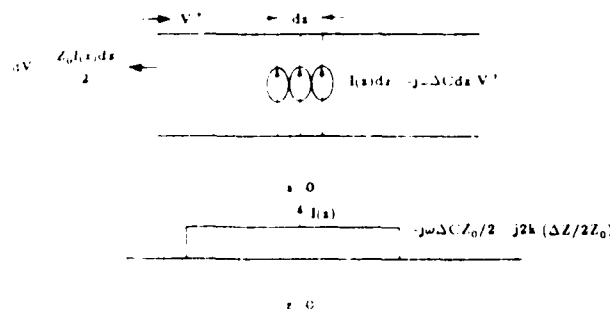

Fig 3 Current induced by incident wave at a mismatched section

$$\frac{\Delta V}{V^+} = j\frac{\Delta Z}{2Z_0}\int_0^{+\theta} e^{j2kz}\,d(2kz) = j\frac{\Delta Z}{Z_0}\sin\theta \quad (6)$$

as before. We note here that the discontinuity in the characteristic impedance is related to the induced current by the relation

$$\frac{\Delta Z}{2Z_0} = \frac{Z_0}{2}(1/2jkV^+) \quad (7)$$

In our problem involving surface waves we will calculate the equivalent I/V^+ and then deduce an equivalent $\Delta Z/2Z_0$ using Eq. 7.

III. Reflection of Surface Acoustic Waves

Surface Acoustic Waves in piezoelectric solids have a fairly complicated pattern of acoustic and electrostatic fields coupled together. The first thing we need to figure out are the "voltages" and "currents." One way to do this is to look at the expression for power flow:

$$P_i = -\frac{1}{2}\{v_x^* T_{xi} + v_y^* T_{yi} + v_z^* T_{zi} - \phi^*(j\omega D_i)\}$$

$$i = x,y,z \quad (8a)$$

$$P = \frac{1}{2}V^*I \quad \text{(Transmission line)} \quad (8b)$$

Here v is the particle velocity, ϕ is the electrostatic potential, D is the electrical displacement and T is the stress. The stress is defined as force per unit area and its two subscripts indicate the direction of the force and the direction of the outward normal to the area. For example, T_{xy} represents the x-directed force per unit area along the xz plane.

Comparing Equations (8a) and (8b) it appears that a surface wave has four pairs of "voltages" and "currents." Usually v_x is zero or negligible and the particle motion is primarily in the sagittal plane (y-z plane, Fig. 1); so we will ignore this component. The electrostatic part can be important if the discontinuity is produced by a conducting electrode and the material has a high piezoelectric constant. This effect, called the piezoelectric scattering, is a different problem altogether, which we will ignore in this paper. In this paper we concentrate on the mechanical reflection due to the component v_y (transverse) and v_z (longitudinal) of the particle motion. Let us look at these one by one.

(a) Impedance Discontinuity due to Transverse Component:

First we consider the particle motion perpendicular to the surface. The induced "current," I in this case, can be identified with T_{yy} that appears on the surface because of the presence of the strip (Fig 1), while the voltage in this case is the particle displacement v_y^+ due to the incident wave. Hence the impedance discontinuity due to the transverse component can be written from Equation (7) as

$$\left.\frac{\Delta Z}{2Z_0}\right|_y = \frac{|v_y|^2}{4P_s}\frac{T_{yy}}{2jkv_y^+} \quad (9)$$

where P_s is the power carried by the surface wave per unit beamwidth, and we have used $|v_y|^2/4P_s$ to replace $Z_0/2 (= V^2/4P)$. We now have to determine T_{yy}/v_y^+. This is done readily, assuming that the strip is a thin one
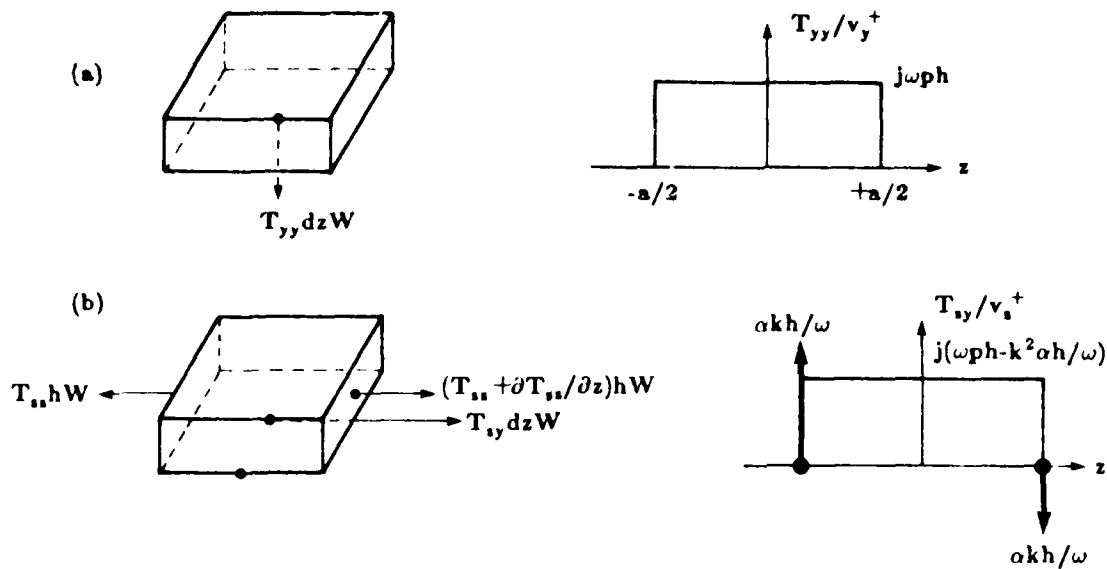
Fig. 4: Stresses induced at strip-substrate interface by an incident surface wave
(a) Transverse Component
(b) Longitudinal Component

so that it merely floats on the wave without loading it. From Newton's law (Fig. 4)

$$T_{yy} \, \dot{a}z \, W = (\rho dzWh) \frac{dv_y^+}{dt}$$

so that

$$\frac{T_{yy}}{v_y^+} = j\omega\rho h \tag{10}$$

Using Equation (10) in Equation (9),

$$\frac{\Delta Z}{2Z_0}\bigg|_y = \frac{|v_y|^2}{4P_a} \cdot \frac{(\rho c_s h)}{2} \tag{11}$$

where $c_s = \omega/k$ is the velocity of the surface wave.

(b) Impedance Discontinuity due to Longitudinal Component:

Arguing as before we can write the impedance discontinuity due to the longitudinal component as

$$\frac{\Delta Z}{2Z_0}\bigg|_z = \frac{|v_z|^2}{4P_a} \cdot \frac{T_{zy}}{2jkv_z^+} \tag{12}$$

Determining T_{zy}/v_z^+, however, is complicated by the fact that the forces on the side faces due to the stress T_{zz} have to be taken into account (Fig. 4). A similar component due to T_{yz} was ignored in Fig. 5a because T_{yz} is zero at the top surface of the strip, and its first order value in the strip can be taken as zero. T_{zz}, on the other hand, is not zero at the top surface. From Newton's law (Fig. 4b),

$$T_{zy}dzW + \frac{\partial T_{zz}}{\partial z} \cdot Whdz = (\rho dzWh)\frac{\partial v_z^+}{\partial t} \tag{13a}$$

$$\frac{T_{zy}}{v_z^+} = j\omega\rho h + jkh \, T_{zz}/v_z^+ \tag{13b}$$

where we have replaced $\partial/\partial z$ by $-jk$. If the strip material is isotropic with Lamé constants λ and μ, it can be shown that

$$\frac{T_{zz}}{v_z^+} = -\frac{\alpha k}{\omega} \tag{14}$$

where $\alpha = \frac{4\mu(\lambda+\mu)}{\lambda+2\mu}$ is an effective stiffness coefficient. If the strip material is not isotropic, the expression for α is more complicated [5]; however, if the strip material is the same as that of the substrate then we can assume that T_{zz} is the same as that for an unperturbed surface wave and calculate α. Using Eq. (14) in Eq. (13b),

$$\frac{T_{zy}}{v_z^+} = j\omega\rho h - jk^2\alpha h/\omega \tag{15}$$

Using Eq. (15) in Eq. 812) we get,

$$\frac{\Delta Z}{2Z_0}\bigg|_z = \frac{|v_z|^2}{4P_a}\left[\frac{\rho c_s h}{2} - \frac{\alpha h}{2c_s}\right] \tag{16'}$$

However, this result is not quite right. The reason is that in going from Eq. (13a) to Eq. (13b) we replaced $\frac{\partial}{\partial z}$ by $-jk$. This is correct within the strip, but at the edges of the strip T_{zz} must go to zero. If we assume (as a first order approximation) that T_{zz} is constant within the strip but goes to zero abruptly at the edges, then the term $\partial T_{zz}/\partial_z$ also gives rise to delta function stresses at the two edges of magnitude $(\alpha kh/\omega)\cdot v_z^+$, which we have neglected. These produce an additional impedance discontinuity of

$$\frac{\Delta Z}{2Z_0}\bigg|_z'' = \frac{|v_z|^2}{4P_a} \cdot \frac{\alpha h}{c_s} \tag{16''}$$

Adding Equations (16') and (16'') we get the total impedance discontinuity due to the longitudinal component.

$$\frac{\Delta Z}{2Z_0}\bigg|_z = \frac{|v_z|^2}{4P_a}\{\frac{\rho c_s h}{2} + \frac{\alpha h}{2c_s}\} \quad (16)$$

(c) Total Impedance Discontinuity

We can now obtain the total impedance discontinuity from the components $\frac{\Delta Z}{2Z_0}\big|_y$ (Eq. 11) and $\frac{\Delta Z}{2Z_0}\big|_z$ (Eq. 16). However, we have to remember that the phases of v_y and v_z are not related in the same way for the incident and reflected waves. For example, if $v_y \sim jv_z$ for the incident wave, then $v_y \sim -jv_z$ for the reflected wave. This can be understood easily if the crystal is reflection symmetric, that is, $+z$ looks the same as $-z$. In that case the fields of the reflected wave can be determined from those of the incident wave simply by turning the z axis around ($z \rightarrow -z$). It is clear that changing $z \rightarrow -z$ changes the sign of v_z but does not affect v_y. Hence $v_y^+/v_z^+ = -v_y/v_z$, where the superscripts + and – refer to incident and reflected waves, respectively.

Because of this change in sign, the net impedance discontinuity is actually the *difference* between $\frac{\Delta Z}{2Z_0}\big|_y$ and $\frac{\Delta Z}{2Z_0}\big|_z$.

$$\frac{\Delta Z}{2Z_0} = \frac{\Delta Z}{2Z_0}\bigg|_y - \frac{\Delta Z}{2Z_0}\bigg|_z \quad (17)$$

The overall sign in Eq. (17) depends on whether we define the reflection coefficient as $\Delta v_y/v_y^+$ or as $\Delta v_z/v_z^+$. Usually we are interested in the reflection coefficient $\Delta\varphi/\phi^+$ because we like to place our transducers at the peak potential of the standing wave. Since ϕ, like v_y, is unaffected by the transformation $z \rightarrow -z$, we expect $\Delta\varphi/\phi^+ = \Delta v_y/v_y^+ = -\Delta v_z/v_z^+$. This is why we have chosen the sign in Eq. 17 to give us the correct sign for $\Delta v_y/v_y^+$ and hence for $\Delta\varphi/\phi^+$. From Equations (11), (16) and (17),

$$\frac{\Delta Z}{2Z_0} = \frac{|v_y|^2}{4P_a}\frac{\rho c_s h}{2} - \frac{|v_z|^2}{4P_a}\{\frac{\rho c_s h}{2} + \frac{\alpha h}{2c_s}\} \quad (18)$$

The reflection coefficient from a strip of length a is given by

$$r = j\sin(ka)\{\frac{|v_y|^2}{4P_a}\rho c_s h - \frac{|v_z|^2}{4P_a}(\rho c_s h + \frac{\alpha h}{c_s})\} \quad (19)$$

At this point we should note a very important difference with a transmission line. For a transmission line $Z_0 = \sqrt{L/C}$ and $v_0 = \sqrt{1/LC}$ so that if we change C keeping L constant, we expect that

$$\frac{\Delta Z}{2Z_0} = \frac{\Delta v}{2v_0}$$

However, in the case of the surface wave this is *not* true. First, the delta function stresses that we encountered have no effect on velocity, they are equal and opposite at the edge of the strip and cancel each other out. For this reason we should use Equation (16') rather than Equation (16). Secondly, the transverse and longitudinal components *add* rather than subtract, so that

$$\frac{\Delta v}{2v_0} = \frac{|v_y|^2}{4P_a}\frac{\rho c_s h}{2} + \frac{|v_z|^2}{4P_a}\{\frac{\rho c_s h}{2} - \frac{\alpha h}{2c_s}\} \quad (20)$$

Eq. (20) has the simple interpretation that the mass-loading (ρ) tends to slow the wave down while the stiffness tends to speed it up. Comparing with Eq. (19) it is apparent that although the same terms are involved, no such simple interpretation is possible. Moreover, it is clear that discontinuities that produce minimal velocity perturbation do *not* produce minimal reflection, and vice versa. From Equations (19) and (20) we can get a simple relation between $\Delta Z/Z_0$ and $\Delta v/v_0$:

$$(\Delta Z/Z_0) = -(\Delta v/v_0) - (|v_z|^2/4P_a)\cdot 2\rho c_s h \quad (21)$$

IV. Mode Conversion of Surface Acoustic Waves

In layered structures if the top layer is sufficiently thick, there are two surface wave modes called the Rayleigh and Sezawa waves. It is possible to have an incident Rayleigh wave with a reflected Sezawa wave or the other way around. The reflection coefficients can be calculated using the same method as described in Section III with the following modifications:

1. In Equation (9) 2jk is replaced by $j(k^+ + k)$, where k^+ and k are the wavenumbers for the incident and reflected waves. (ω is the same for both.) As a result Eq. (11) becomes

$$\frac{\Delta Z}{2Z_0}\bigg|_y = \frac{|v_y|\,|v_y^+|}{4P_a}\frac{\rho\omega h}{k^+ + k} \quad (22)$$

2. In Equation (15), k^2 is replaced by that of the incident wave $(k^+)^2$, while in Eq. 12, 2k is replaced by $k^+ + k$ so that Equation (16') becomes

$$\frac{\Delta Z}{2Z_0}\bigg|_z' = \frac{|v_z|\,|v_z^+|}{4P_a}\{\frac{\rho\omega h}{k^+ + k} - \frac{\alpha k^{+2}h}{(k^+ + k)\omega}\} \quad (23)$$

while Equation (16'') becomes

$$\frac{\Delta Z}{2Z_0}\bigg|_z'' = \frac{|v_z|\,|v_z^+|}{4P_a}\{\frac{\alpha k^+ h}{\omega}\} \quad (24)$$

From Equations (23) and (24),

$$\frac{\Delta Z}{2Z_0}\bigg|_z = \frac{|v_z|\,|v_z^+|}{4P_a}\{\frac{\rho\omega h}{k^+ + k} + \frac{\alpha h k^+ k}{(k^+ + k)\omega}\} \quad (25)$$

Note that the final result (Eq. 25) is symmetric in k^+ and k though Equations (23) and (24) are not. This symmetry is rather important since the reflection coefficient should be the same regardless of which wave (Rayleigh or Sezawa) is incident and which is reflected. This is required by the principle of reciprocity.

3. To get the overall impedance discontinuity we *add* the individual components. This is because v_y/v_z have different signs for Rayleigh and Sezawa waves traveling in the same direction. As a result a Rayleigh and a Sezawa wave traveling in *opposite* directions have the *same* sign for v_y/v_z.

$$r = j\sin\frac{(k^+ + k)a}{2}\{\frac{|v_y|\,|v_y^+|}{4P_a}\frac{2\rho\omega h}{k^+ + k} + \frac{|v_z|\,|v_z^+|}{4P_a}(-\frac{2\rho\omega h}{k^+ + k} + \frac{2\alpha h k^+ k}{(k^+ + k)\omega})\} \quad (26)$$

V. Examples

(a) Grooves in ST-quartz: For an unperturbed surface wave on ST-quartz,

$$\frac{|v_y|^2}{4P_a} = (4.5 \times 10^{-12} \ \frac{m^2}{nt}) \cdot \omega$$

$$\frac{|v_z|^2}{4P_a} = (1.95 \times 10^{12} \ \frac{m^2}{Nt}) \cdot \omega$$

$$c_s = 3158 \ m/s.$$

An array of grooves may alternatively be viewed as an array of strips made of the same material as the substrate. For strips of ST-quartz,

$$\rho = 2651 \ Kg/m^3.$$

$$\alpha = 8.69 \times 10^{10} \ Nt/m^2$$

From Equation (11).

$$\frac{\Delta Z}{Z_0}\bigg|_y = .75 \ \frac{h}{\lambda}$$

From Equation (16)

$$\frac{\Delta Z}{Z_0}\bigg|_z = (.32 + 1.06) \ \frac{h}{\lambda}$$

From Equation (17),

$$\frac{\Delta Z}{Z_0} = -.63 \ \frac{h}{\lambda}$$

which agrees with the experimental results [6]. Note that, from Eq 20,

$$\frac{\Delta v}{v_0} \simeq 0$$

which is what we expect since the wave velocity is the same under the strip as in the groove.

(b) Grooves in Silicon:

For an unperturbed surface wave on (111) cut ($\bar{2}$11) propagating silicon,

$$\frac{|v_y|^2}{4P_a} = (2.57 \times 10^{-12} \ m^2/Nt.)\omega$$

$$\frac{|v_z|^2}{4P_a} = (1.04 \times 10^{-12} \ m^2/Nt.)\omega$$

$$c_s = 4733 \ m/s.$$

Also for strips of silicon,

$$\rho = 2332 \ kg/m^3$$

$$\alpha = 1.82 \times 10^{11} \ nt/m^2$$

We have as before,

$$\frac{\Delta Z}{Z_0}\bigg|_y = .84 \ \frac{h}{\lambda}$$

$$\frac{\Delta Z}{Z_0}\bigg|_z = (.34 + 1.18) \ \frac{h}{\lambda}$$

$$\frac{\Delta Z}{Z_0} = -.68 \ \frac{h}{\lambda}$$

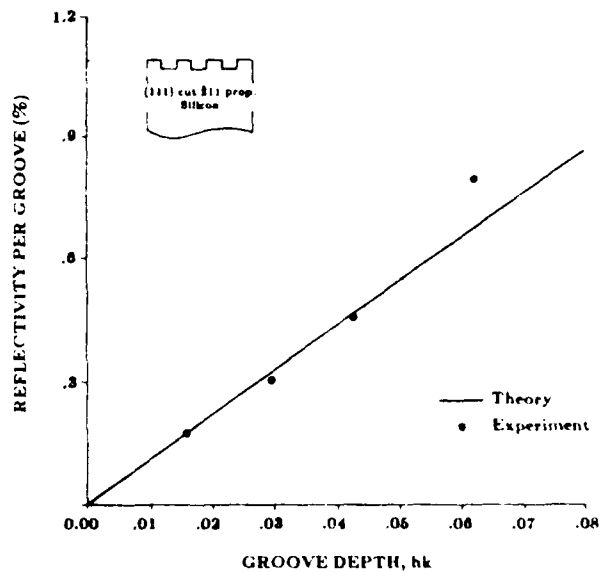This is plotted in Fig. 5 along with the experimental data from Schwartz et al. [7].

Fig. 5: Reflectivity per groove vs groove depth for (111) cut ($\bar{2}$11) prop. silicon. (Experimental data from Ref. 7)

(c) Grooves in SiO$_2$-on-Silicon:

The reflectivity per groove was measured as a function of the groove depth in a layered structure having a 3.08 μm thick layer of SiO$_2$ on a (111) cut ($\bar{2}$11) propagating silicon substrate at λ = 40.6 μm. In this case, we find for the unperturbed surface wave,

$$\frac{|v_y|^2}{4P_a} = (3.31 \times 10^{-12} \ m^2/Nt) \ \omega$$

$$\frac{|v_z|^2}{4P_a} = (2.49 \times 10^{-12} \ m^2/Nt.) \ \omega$$

$$c_s = .023 \ m/s.$$

For strips of SiO$_2$,

$$\rho = 2300 \ Kg/m^3$$

$$\alpha_s = 7.52 \times 10^{10} \ Nt/m^2$$

$$\frac{\Delta Z}{Z_0}\bigg|_y = .95 \ \frac{h}{\lambda} \qquad \frac{\Delta Z}{Z_0}$$

$$\frac{\Delta Z}{Z_0}\bigg|_z = (.72 + 1.2) \ \frac{h}{\lambda}$$

$$\frac{\Delta Z}{Z_0} = -.97 \ \frac{h}{\lambda}$$

$$\frac{\Delta v}{v_0} = -.47 \ \frac{h}{\lambda}$$

Note that $\frac{\Delta v}{v_0}$ is not zero in this case because of the dispersive nature of layered structures. Fig. 6 shows the theoretically predicted $\Delta Z/Z_0$ and the experimentally measured values from Ref. 7

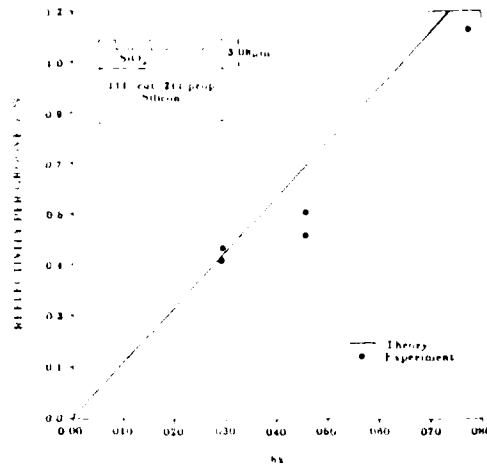(e) Mode Conversion in ZnO-on-SiO$_2$-on-silicon by grooves

Fig. 6. Reflectivity per groove vs. groove depth for SiO_2 on (111) cut ($\overline{2}11$) prop. silicon. (Experimental data from Ref. 7)

Fig. 7. Mode Conversion reflectivity (Sezawa to Rayleigh) for ZnO on SiO_2 on (100) cut (010) prop. silicon. (*Experimental data from Refs. 4,9*)

The mode conversion reflectivity (from Sezawa to Rayleigh) was measured in ZnO (7.6 μm thick) on SiO_2 (.25 μm) on (100) cut (010) propagating silicon. For the unperturbed Rayleigh and Sezawa waves we find,

$$\frac{|v_y|^2}{4P_a} = (5.9 \times 10^{-12} \text{ m}^2/\text{Nt.})\ \omega \quad \text{Rayleigh}$$

$$(8.3 \times 10^{-12} \text{ m}^2/\text{Nt.})\ \omega \quad \text{Sezawa}$$

$$\frac{|v_z|^2}{4P_a} = (1.53 \times 10^{-12} \text{ m}^2/\text{Nt.})\ \omega \quad \text{Rayleigh}$$

$$(1.53 \times 10^{-12} \text{ m}^2/\text{Nt.})\ \omega \quad \text{Sezawa}$$

Also for ZnO strips,

$$\rho = 5680 \text{ kg/m}^3$$

$$\alpha = 1.6 \times 10^{11} \text{ Nt/m}^2$$

Hence from Eq. 25 with $\omega = 2\pi \times 152.4$ MHz, $k^+ = 18$ μm^{-1} $k^- = .32$ μm^{-1} and $(k^+ + k^-)a = \pi$,

$$r = j\ 1.34 \times 10^{-2}\ h(\text{in Å})$$

Fig. 7 shows the theoretical reflection coefficient and the experimentally measured values [4,9].

(f) Bimetal Electrodes for Zero Reflection.

It is apparent from Eq. 18 that the impedance discontinuity may be either positive or negative though, in most cases it is negative. One notable exception is gold which because of its high mass-density ρ often gives rise to a positive $\Delta Z/Z_0$. For gold strips,

$$\rho = 19300 \text{ Kg/m}^3$$

$$\alpha = 9.8 \times 10^{10} \text{ Nt/m}^2$$

$$\rho = 7200 \text{ kg/m}^3$$
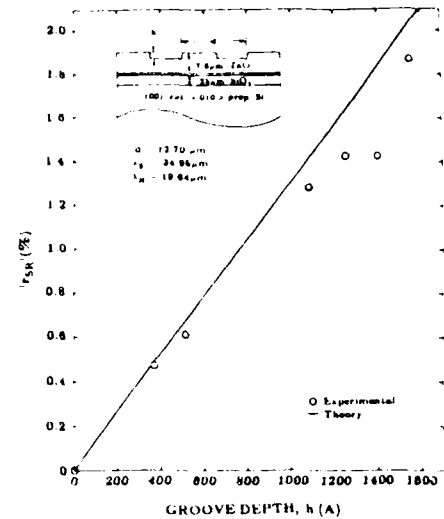
$$\alpha = 2.82 \times 10^{11} \text{ Nt/m}^2$$

For an ST quartz substrate,

$$\frac{\Delta Z}{Z_0}\bigg|_y = 5.41\ \frac{h}{\lambda} \quad \text{(gold)}$$

$$= 2.03\ \frac{h}{\lambda} \quad \text{(chromium)}$$

$$\frac{\Delta Z}{Z_0}\bigg|_x = (2.36 + 1.2)\ \frac{h}{\lambda} \quad \text{(gold)}$$

$$= (.88 + 3.46)\ \frac{h}{\lambda} \quad \text{(chromium)}$$

$$\frac{\Delta Z}{Z_0} = 1.88\ \frac{h}{\lambda} \quad \text{(gold)}$$

$$= -2.31\ \frac{h}{\lambda} \quad \text{(chromium)}$$

It thus seems feasible to fabricate a bimetal reflectionless electrode with about 55% gold and 45% chromium. A similar prediction (90% gold, 10% chromium) has been qualitatively verified for a 100 cut, 110 propagating GaAs substrate, but not quantitatively. A possible reason for the discrepancy is the uncertainty in the elastic constants of thin films as explained in Ref. 8.

VI. Conclusions.

In this paper we have presented a simple approach to the first-order mechanical reflection caused by grooves and electrodes. The theory is developed by analogy with transmission lines (rigorous derivations based on the normal mode theory have been presented elsewhere) and the similarities and differences are discussed. The theoretical results agree well with experimental data for various single crystal and layered substrates.

VII. Acknowledgements.

VIII. References:

1. B. A. Auld, *Acoustic Fields and Waves in Solids* (Wiley - Interscience, New York, 1973), Vol. II, pp. 275-283 and 302-309.

2. D. A. Simons, J. Acoust. Soc. Am. *63*, 1292 (1978).

3. S. Datta and B. J. Hunsinger, "First-order Reflection Coefficient of Surface Acoustic Waves from Thin-Strip Overlays," J. Appl. Phys. *50* (9), 5661 (1979).

   B. J. Hunsinger, Final Report to RADC, RADC-TR-81-73.

4. S. Bandyopadhyay, S. Datta, S. J. Martin and R. L. Gunshor, "Coherent Mode Conversion by Grooved Arrays in Layered Media," to appear in J. Appl. Phys. Jan 1984.

5. See Ref. 1.

6. C. Dunnrowicz, F. Sandy and T. Parker, "Reflection of Surface Waves from Periodic Discontinuities," IEEE Ultrasonics Symposium Proceedings, Cat. No. 76CH1120-5SU, 386 (1976).

7. S. S. Schwartz, S. J. Martin, R. L. Gunshor, S. Datta and R. F. Pierret, "SAW Resonators on Silicon with ZnO Limited to IDT Regions," IEEE Ultrasonics Symposium Proceedings, this issue.

8. E. G. Bogus, M. J. Hoskins and B. J. Hunsinger, "Cancelling Surface Acoustic Wave Reflections from Metallic Strips Using a Bimetal Geometry," to appear in IEEE Trans. on Sonics and Ultrasonics.

9. S. J. Martin, R. L. Gunshor, M. R. Melloch, S. Datta and R. F. Pierret, "Surface Acoustic Wave Mode Conversion Resonator," Appl. Phys. Lett. *43*, 238 (1983).

Coherent mode conversion by grooved arrays in layered media

S. Bandyopadhyay, S. Datta, S. J. Martin, and R. L. Gunshor

School of Electrical Engineering, Purdue University, W. Lafayette, Indiana 47907

Recent experiments have shown that a periodic array of grooves and strips on a layered medium provides efficient conversion between Rayleigh and Sezawa modes supported by the medium; these novel mode converting reflectors have been used to construct surface wave resonators. This paper presents a theoretical analysis of the mode conversion process starting from material parameters. A first-order perturbation theory is used to construct a four-port scattering matrix for each strip in the array. The scattering matrices are then converted to transmission matrices and cascaded to provide the overall scattering characteristics of the array. The predicted characteristics are in close agreement with experimentally measured values.

I. INTRODUCTION

It is known that two surface acoustic modes (Rayleigh and Sezawa) can propagate in a layered medium of sufficient thickness. Recently, it has been demonstrated that an array of grooves and strips with the right periodicity produces a reflected Rayleigh wave in response to an incident Sezawa wave and vice versa.[1] Two such mode-converting reflectors have been used to form a resonator cavity with a $Q \approx 3000$, showing that the mode conversion is quite efficient.[2,3] This paper treats the mode conversion process using a first order perturbation approach.

We describe a theoretical analysis of the scattering characteristics of a periodic array of grooves, starting from material parameters. The predicted characteristics are in close agreement with experimentally measured values. The approach used is to describe each strip in the array as a four-port scattering junction having two Rayleigh ports and two Sezawa ports. The elements of the 4×4 scattering matrix are determined from material parameters using first-order perturbation theory (Sec. II). The scattering matrices are then converted to transmission matrices and cascaded to provide the overall scattering characteristics of the array (Sec. III).

It will be noted that conventional reflecting arrays involve a single mode and are described by a 2×2 scattering matrix. Mode-converting arrays on the other hand involve two modes and require a 4×4 scattering matrix. In many practical cases, however, it may be possible to use a 2×2 scattering matrix description. For example, suppose the array period is such that at a particular frequency an incoming Sezawa wave traveling to the right is phase matched to a Rayleigh wave traveling to the left but not to the left-going Sezawa or the right-going Rayleigh. At this frequency it may be permissible to ignore the two waves which are not phase matched and use a 2×2 scattering matrix. The validity of this procedure will depend on the length of the array and the degree of phase mismatch. In this paper we use a general description based on a 4×4 scattering matrix.

II. SCATTERING CHARACTERISTICS OF A SINGLE STRIP

A. First-order perturbation theory

Consider a single strip on the surface of a layered medium [Fig. 1(a)]. An incident wave induces a set of stresses at the interface $(T^s_{yy}, T^s_{xy}, T^s_{zy})$ which then act as the sources for the scattered Rayleigh and Sezawa waves [Fig. 1(b)]. The overall problem can thus be divided into two parts: (1) to determine the induced stress $T^s (T^s_{yy}, T^s_{xy}, T^s_{zy})$ for a given incident wave, and (2) to determine the amplitudes of the scattered waves generated by the induced source T^s. The second part is treated first.

Consider a wave with an amplitude $A(z) \exp(-j\beta z)$. The growth of the wave in the presence of the source T^s is described by

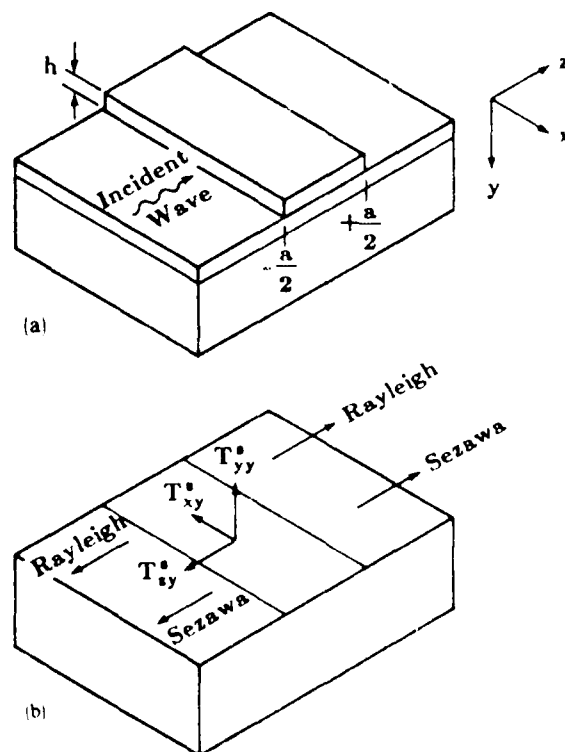$$\frac{dA}{dz} = \frac{(v e^{-j\beta z})^* \cdot T^s}{4P/W}, \qquad (1)$$

(a)

(b)

where $A e^{-j\beta z}\mathbf{v}$ is the particle velocity at the surface and $A^2 P$ is the total power carried by a wave of amplitude A and width W (in the x direction). This result is derived rigorously starting from the reciprocity theorem.[4] However, a simple argument can be used to show its plausibility. The power flow from the source into the wave over a length dz is given by

$$\frac{1}{2}(A e^{-j\beta z}\mathbf{v})^{*}\cdot\mathbf{T}^{s}\, W dz.$$

This means a fractional change in power of

$$\frac{(A e^{-j\beta z}\mathbf{v})^{*}\cdot\mathbf{T}^{s}\, W dz}{2A A^{*}P}.$$

Since the power is proportional to the amplitude squared, the fractional change in amplitude is equal to half the fractional change in power.

$$\frac{dA}{A} = \frac{(A e^{-j\beta z}\mathbf{v})^{*}\cdot\mathbf{T}^{s}\, W dz}{4 A A^{*}P}.$$

Simplifying, one obtains Eq. (1).

The first part of the problem is then to determine $\mathbf{T}^{s}$ for a given incident wave. This aspect of the problem is discussed in Ref. 5 where it is shown that the interface stress is proportional to particle velocity at the surface associated with the incident wave.

$$T^{s}_{xx} = A_i e^{-j\beta_i z} v^i_x\, \frac{h}{\omega} f_x(z),$$

$$T^{s}_{yx} = A_i e^{-j\beta_i z} v^i_y\, \frac{h}{\omega} f_y(z), \qquad (2)$$

$$T^{s}_{zx} = A_i e^{-j\beta_i z} v^i_z\, \frac{h}{\omega} f_z(z),$$

where $A_i e^{-j\beta_i z}\mathbf{v}$ is the particle velocity due to the incident wave of amplitude $A_i \exp(-j\beta_i z)$. The superscript or subscript i refers to incident wave parameters and ω is the angular frequency. The functions f_x, f_y, and f_z are constants over the region of the strip $(-a/2 < z < a/2)$ and zero elsewhere. They are defined below. It is of interest to note that f_x and f_z have two delta functions at the edges of the strip.[5]

$$f_x(z) = j\omega^2\rho - j\beta_i^2\alpha_x + \alpha_x\beta_i$$
$$\times \left[\delta\!\left(z + \frac{1}{2}a\right) - \delta\!\left(z - \frac{1}{2}a\right)\right],$$

$$f_y(z) = j\omega^2\rho, \qquad (3)$$

$$f_z(z) = j\omega^2\rho - j\beta_i^2\alpha_z + \alpha_z\beta_i$$
$$\times \left[\delta\!\left(z + \frac{1}{2}a\right) - \delta\!\left(z - \frac{1}{2}a\right)\right].$$

ρ, α_x, and α_z are constants characterizing the strip material. ρ is the mass density while α_x, α_z are effective stiffness coefficients. If the strip is made of an isotropic material with Lamé constants λ and μ, then

$$\alpha_x = \mu,$$

$$\alpha_z = \frac{4\mu(\lambda + \mu)}{\lambda + 2\mu}. \qquad (4)$$

For an anisotropic strip, the expressions for α_x, α_z are[6]

$$\alpha_x = S^i_1/D,$$
$$\qquad (5)$$
$$\alpha_z = S^3_3/D,$$

where

$$D = S^3_3 S^1_1 - S^3_1 S^1_3,$$

and

$$S^i_j = (s_{i1}s_{ij} - s_{ij}s_{i1})/s_{11},$$

s_{ij} being the compliance tensor. In general the situation is more complicated than Eq. (2) indicates, with T^s_{xx} depending on v_z and T^s_{zx} on v_x. However, v_x is usually zero or negligible so that neglecting the dependence on v_x does not cause serious discrepancy.

Using Eq. (2) in Eq. (1) we have

$$\frac{1}{A_i}\frac{dA}{dz} = h(c_x f_x + c_y f_y + c_z f_z)e^{-j(\beta_i - \beta)z}, \qquad (6)$$

where

$$c_x = \frac{v^*_x v^i_x}{4 P\omega/W},$$

$$c_y = \frac{v^*_y v^i_y}{4 P\omega/W}, \qquad (7)$$

$$c_z = \frac{v^*_z v^i_z}{4 P\omega/W}.$$

Integrating Eq. (6) over the region of the strip one obtains the ratio of the amplitude of the scattered wave (ΔA) to that of the incident wave (A_i).

$$\frac{\Delta A}{A_i} = h\left[c_x I_x + c_y I_y + c_z I_z\right], \qquad (8)$$

where

$$I_x = \int_{-a/2}^{+a/2} f_x(z) e^{-j(\beta_i - \beta)z} dz,$$

$$= j\sin\frac{1}{2}(\beta_i - \beta)a\left[\frac{\rho\omega^2 - \alpha_x\beta_i\beta}{\frac{1}{2}(\beta_i - \beta)}\right],$$

$$I_y = j\sin\frac{1}{2}(\beta_i - \beta)a\,\frac{\rho\omega^2}{\frac{1}{2}(\beta_i - \beta)},$$

$$I_z = j\sin\frac{1}{2}(\beta_i - \beta)a\left[\frac{\rho\omega^2 - \alpha_z\beta_i\beta}{\frac{1}{2}(\beta_i - \beta)}\right].$$

B. Scattering matrix for a single strip

A single strip in a grooved array mode converting reflector is treated as a four-port network, as shown in Fig. 2. The quantities a represent the input modes and the quantities b represent the output (reflected or transmitted) modes. The representation S stands for Sezawa modes and R stands for Rayleigh modes in the figure.

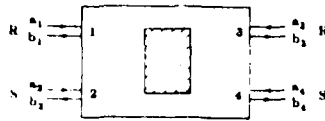The scattering matrix[7] is defined as the matrix relating the b's to the a's:

FIG. 2. Four port scattering network for a single strip or groove

$$\begin{bmatrix} b_1 \\ b_2 \\ b_3 \\ b_4 \end{bmatrix} = \begin{bmatrix} S_{11} & S_{12} & S_{13} & S_{14} \\ S_{21} & S_{22} & S_{23} & S_{24} \\ S_{31} & S_{32} & S_{33} & S_{34} \\ S_{41} & S_{42} & S_{43} & S_{44} \end{bmatrix} \begin{bmatrix} a_1 \\ a_2 \\ a_3 \\ a_4 \end{bmatrix},$$

or in matrix notation

$$|b| = [S]|a|. \tag{9}$$

For a reciprocal device, the principle of reciprocity gives[7]

$$S_{ij} = S_{ji} \quad i,j = 1,2,3,4.$$

Using r_{mn} for the reflection coefficient from mode m to mode n (m and n traveling in opposite directions), and K_{mn} for the conversion coefficient from mode m to mode n (m and n traveling in the same direction), we may write

$$S_{11} = S_{33} = r_{RR}, \tag{10}$$

$$S_{22} = S_{44} = r_{SS}, \tag{11}$$

$$S_{12} = S_{34} = r_{RS} = S_{21} = S_{43} = r_{SR}, \tag{12}$$

$$S_{14} = S_{32} = K_{RS} = S_{41} = S_{23} = K_{SR}, \tag{13}$$

$$S_{13} = S_{31} = 1 + j\xi_R, \tag{14}$$

$$S_{24} = S_{42} = 1 + j\xi_S, \tag{15}$$

where the subscript R stands for Rayleigh mode and S for Sezawa mode.

The coefficients ξ_R and ξ_S need some clarification. Normally in this lossless network, an input mode would pass through unattenuated and emerge as such, so that $S_{11} = S_{33} = S_{24} = S_{42} = 1$. Because of the perturbation caused by the strip, the incident wave suffers a phase shift equal to $\xi_{R,S}$. The amplitude must also decrease in order to satisfy power conservation; however, the decrease is of order $\sim r^2$ (r being the reflection coefficient) and is not given by first-order perturbation theory. For a single strip this represents a small error but the error may build up when calculating the characteristics of an array. Energy conservation can be ensured by requiring that the S matrix satisfy the condition.

$$[S^*]'[S] = [I], \tag{16}$$

where $[I]$ is the identity matrix. This is ensured if we divide each S matrix element S_{ij} by $[\Sigma_i |S_{ij}|^2]^{1/2}$.

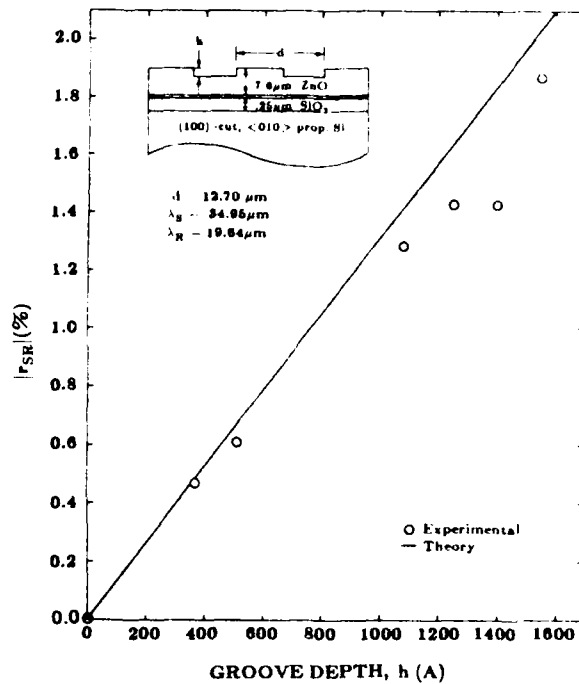Experimental measurements were performed on the

FIG. 3. Magnitude of Sezawa-to-Rayleigh mode scattering vs groove depth in the ZnO layer.

ZnO-Al-SiO$_2$-Si structure shown in Fig. 3. The grooves were ion milled and a uniform mark to space ratio of unity was maintained. For the dimensions shown, the Rayleigh and Sezawa wave (phase) velocities are 2993 and 5326 m/s, respectively. At a measurement frequency of 152.4 MHz, the corresponding wave numbers are

$$\beta_R = 0.32 \ \mu m^{-1} (\lambda_R = 19.64 \ \mu m),$$

$$\beta_S = 0.18 \ \mu m^{-1} (\lambda_S = 34.95 \ \mu m)$$

The particle velocities at the surface for different waves are shown in Table I, all normalized to 1 W/m of beam width. These were obtained from a computer program that determines the velocity and field distributions of surface waves in layered media.

R$^+$ refers to incident or transmitted forward traveling wave and R$^-$ refers to the reflected reverse traveling Rayleigh wave. Similarly S$^+$ and S$^-$ denote forward and reverse traveling Sezawa waves. The strip material in this case is ZnO for which we have (Eq. 5)

$$\rho = 5680 \ kg/m^3,$$

$$\alpha_x = 0$$

$$\alpha_z = 1.6 \times 10^{11} \ N/m^2.$$

TABLE I Surface particle velocities (in m/s) normalized to 1 W/m

	R$^+$	R$^-$	S$^+$	S$^-$
V_x	0	0	0	0
V_y	$-j1.57 \times 10^{-10} \omega$	$-j1.57 \times 10^{-10} \omega$	$+j0.59 \times 10^{-10} \omega$	$+j0.59 \times 10^{-10} \omega$
V_z	$0.8 \times 10^{-10} \omega$	$-0.8 \times 10^{-10} \omega$	$0.8 \times 10^{-10} \omega$	$0.8 \times 10^{-10} \omega$

Using Eq. (8), we obtain the scattering elements (h is in units of angstroms)

$$S_{11} = S_{33} = \frac{\Delta A\,(R^-)}{A_i(R^+)} = -j5.55 \times 10^{-7}h,$$

$$S_{22} = S_{44} = \frac{\Delta A\,(S^-)}{A_i(S^+)} = -j5.79 \times 10^{-6}h,$$

$$S_{12} = S_{21} = S_{34} = S_{43} = \frac{\Delta A\,(S^-)}{A_i(R^+)}$$

$$= \frac{\Delta A\,(R^-)}{A_i(S^+)} = -j1.329 \times 10^{-5}h,$$

$$S_{14} = S_{41} = S_{23} = S_{32} = \frac{\Delta A\,(S^+)}{A_i(R^+)}$$

$$= \frac{\Delta A\,(R^+)}{A_i(S^-)} = -j1.07 \times 10^{-5}h,$$

$$S'_{11} = S'_{33} = 1 + \frac{\Delta A\,(R^+)}{A_i(R^+)} \approx 1 + j8.67 \times 10^{-6}h,$$

$$S'_{24} = S'_{42} = 1 + \frac{\Delta A\,(S^+)}{A_i(S^+)} = 1 + j2.67 \times 10^{-6}h.$$

Figure 3 shows good agreement between theoretically predicted values of $S_{21}(= S_{12} = S_{34} = S_{43}]$ and experimentally measured values. The agreement deteriorates at higher values of h, which probably shows the inadequacy of the first order model for large groove depth. The first order model predicts a reflection coefficient linearly proportional to h and neglects higher order contributions. At small values of h, the linear term dominates, but the effect of higher order terms becomes more pronounced with higher values of h.

III. SCATTERING MATRIX OF A GROOVED ARRAY

A. Cascading procedure

When treating the entire array of grooves, the transmission matrix is more useful since the transmission characteristic for the entire array can be deduced by merely multiplying together the individual transmission matrices.

With reference to Fig. 2, the transmission matrix is defined as

$$\begin{bmatrix} a_3 \\ a_4 \\ b_3 \\ b_4 \end{bmatrix} = \begin{bmatrix} T_{11} & T_{12} & T_{13} & T_{14} \\ T_{21} & T_{22} & T_{23} & T_{24} \\ T_{31} & T_{32} & T_{33} & T_{34} \\ T_{41} & T_{42} & T_{43} & T_{44} \end{bmatrix} \begin{bmatrix} a_1 \\ a_2 \\ b_1 \\ b_2 \end{bmatrix}.$$

The individual transmission matrix elements can be found from the scattering matrix elements with the help of the relationships given in the Appendix. The scattering matrix elements are determined in Sec. II, assuming that the wave amplitudes are all referred to the center of the strip. However, for purposes of cascading it is better to have a_1, a_2, b_1, b_2 referred to the output plane and a_3, a_4, b_3, b_4 referred to the input plane. This can be done by multiplying $S_{11}, S_{13}, S_{31}, S_{33}$ by $\exp(-j\beta_R l)$, $S_{22}, S_{24}, S_{42}, S_{44}$ by $\exp(-j\beta_S l)$ and all other terms by $\exp(-j\beta_R l - j\beta_S l)$, where l is the center-to-center distance between successive grooves.

Before performing the final operation of cascading, a glance at Fig. 4 will reveal that merely multiplying the trans-
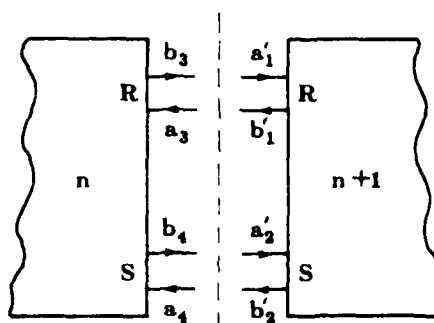

FIG. 4. Cascading of two successive scattering networks.

mission matrices will not achieve the desired purpose. This is because the outgoing quantities from the first network are b_3 and b_4 whereas the ingoing quantities into the second network are a'_1, a'_2 rather than b'_1, b'_2. Hence, in order to achieve the desired cascading, the outgoing b's of the first network must be transformed to ingoing a's of the second network and vice versa. This is easily achieved by introducing a transformation matrix $[V]$ defined by

$$\begin{bmatrix} a'_1 \\ a'_2 \\ b'_1 \\ b'_2 \end{bmatrix} = \begin{bmatrix} V \end{bmatrix} \begin{bmatrix} a_3 \\ a_4 \\ b_3 \\ b_4 \end{bmatrix},$$

where

$$[V] = \begin{bmatrix} 0 & 0 & 1 & 0 \\ 0 & 0 & 0 & 1 \\ 1 & 0 & 0 & 0 \\ 0 & 1 & 0 & 0 \end{bmatrix}.$$

The cascading may now be performed as

$$[T]_{\text{eff}} = [T]_n [V][T]_{n-1} \cdots [V][T]_1,$$

where n is the number of strips, $[T]$ the transmission matrix for any one strip, and $[T]_{\text{eff}}$ the overall transmission matrix for the entire array.

Next the overall transmission matrix is converted back into a scattering matrix by using the same relationships as in the Appendix with T's and S's interchanged.

B. Discussion

Figure 5 demonstrates the excellent agreement between experimentally measured and theoretically calculated values of $|S_{42}|$ (the magnitude of the ratio the transmitted Sezawa wave to input Sezawa wave for the entire array) as a function of frequency. The same device as previously described was used and the number of strips was 200. The magnitude of the dip at the center frequency was computed to be -17.4 dB while it was experimentally measured as -16.5 dB. The magnitude of this dip depends on the groove depth and increases with h.

Another difference between theory and experiment discerned in the plots is that the experimental curve continuously "droops" as one goes farther from the center frequen-
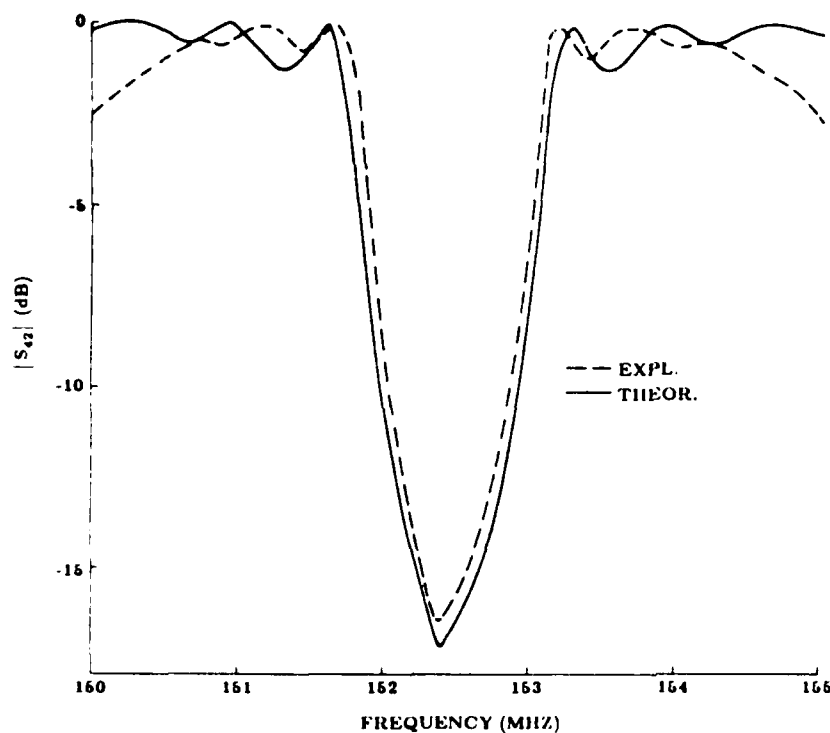
FIG. 5. Theoretical and experimental plot of $|S_{42}|$ vs frequency ($h = 1088$ Å).

- - - EXPL.
—— THEOR.

cy. This is caused by the transducer (IDT) frequency response and has nothing to do with the mode conversion.

Figures 6 and 7 show the theoretical plots of $|S_{12}|$ and S_{22} versus frequency. The plot of S_{12} is most interesting since at the center frequency, $1/2 (\beta_R + \beta_S) a = \pi/2(a =$ strip width $= 1/2 \times$ period of array) so that the reflected Rayleigh waves add in phase. This constructive interference causes the plot of S_{12} to peak at 152.4 MHz. For the same reason the plot of $|S_{42}|$ dips at 152.4 MHz. The plot of S_{22} (Fig. 7) shows no interesting features. This is because Fig. 7 plots the reflected Sezawa wave in response to an incident

Sezawa wave. These two waves are not phase matched at the chosen frequency and array periodicity; hence, they interfere destructively and decay out. (This is why the levels are 40 dB down). However, if the frequency and array periodicity were such that $\beta_S a = \pi/2$, then this plot would show essentially the same features as Fig. 6.

IV. CONCLUSION

In this paper we have presented a theoretical analysis based on a first order model for mode conversion between Sezawa and Rayleigh modes produced by scattering in
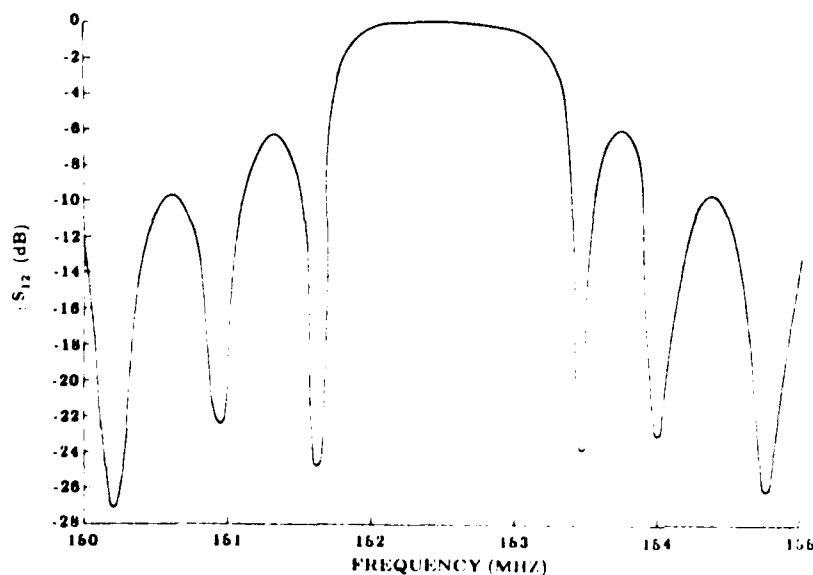

FIG. 6. Theoretical plot of S_{12} vs frequency ($h = 1088$ Å).
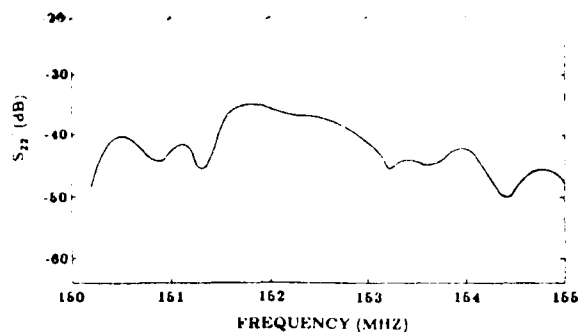
FIG. 7 Theoretical plot of $|S_{22}|$ vs frequency $(h = 1088 \text{ Å})$.

grooved arrays. The predicted conversion coefficient per strip and the overall transmission characteristics over a broad range of frequencies are in excellent agreement with experimental results. This indicates that the first-order model presented here adequately describes the behavior of grooved arrays for reasonably small groove depths.

ACKNOWLEDGMENT

APPENDIX

Relationships between transmission matrix elements and scattering matrix elements for a four-port network. The following equations express T's in terms of S's. The S's in terms of T's are obtained by interchanging S's and T's.

$$T_{11} = \frac{S_{14}S_{21} - S_{24}S_{11}}{S_{13}S_{24} - S_{23}S_{14}},$$

$$T_{12} = \frac{S_{14}S_{22} - S_{24}S_{12}}{S_{13}S_{24} - S_{23}S_{14}},$$

$$T_{13} = \frac{S_{24}}{S_{13}S_{24} - S_{23}S_{14}},$$

$$T_{14} = \frac{-S_{14}}{S_{13}S_{24} - S_{23}S_{14}},$$

$$T_{21} = \frac{S_{23}S_{11} - S_{13}S_{21}}{S_{13}S_{24} - S_{23}S_{14}},$$

$$T_{22} = \frac{S_{23}S_{12} - S_{13}S_{22}}{S_{13}S_{24} - S_{23}S_{14}},$$

$$T_{23} = \frac{-S_{23}}{S_{13}S_{24} - S_{23}S_{14}},$$

$$T_{24} = \frac{S_{13}}{S_{13}S_{24} - S_{23}S_{14}},$$

$$T_{31} = S_{31} + \frac{S_{33}(S_{14}S_{21} - S_{24}S_{11}) + S_{34}(S_{23}S_{11} - S_{13}S_{21})}{S_{13}S_{24} - S_{23}S_{14}},$$

$$T_{32} = S_{32} + \frac{S_{33}(S_{14}S_{22} - S_{24}S_{12}) + S_{34}(S_{23}S_{12} - S_{13}S_{22})}{S_{13}S_{24} - S_{23}S_{14}},$$

$$T_{33} = \frac{S_{33}S_{24} - S_{23}S_{34}}{S_{13}S_{24} - S_{23}S_{14}},$$

$$T_{34} = \frac{S_{14}S_{33} - S_{33}S_{14}}{S_{13}S_{24} - S_{23}S_{14}},$$

$$T_{41} = S_{41} + \frac{S_{43}(S_{14}S_{21} - S_{24}S_{11}) + S_{44}(S_{23}S_{11} - S_{13}S_{21})}{S_{13}S_{24} - S_{23}S_{14}},$$

$$T_{42} = S_{42} + \frac{S_{43}(S_{14}S_{22} - S_{24}S_{12}) + S_{44}(S_{23}S_{12} - S_{13}S_{22})}{S_{13}S_{24} - S_{23}S_{14}},$$

$$T_{43} = \frac{S_{24}S_{43} - S_{23}S_{44}}{S_{13}S_{24} - S_{23}S_{14}},$$

$$T_{44} = \frac{S_{13}S_{44} - S_{43}S_{14}}{S_{13}S_{24} - S_{23}S_{14}}.$$

[1] M. R. Melloch, R. L. Gushor, and R. F. Pierret, Appl. Phys. Lett. 39, 476, (1981).

[2] S. J. Martin, S. Datta, R. L. Gunshor, R. F. Pierret, M. R. Melloch, and E. J. Staples, IEEE Ultrason. Symp. Proc. 290, Cat. No. 82CH1823-4 (1982).

[3] S. J. Martin, R. L. Gunshor, M. R. Melloch, S. Datta, and R. F. Pierret, Appl. Phys. Lett. 43, 238 (1983).

[4] B. A. Auld, *Acoustic Fields and Waves in Solids* (Wiley-Interscience, New York, 1973), Vol. II, pp. 275–283 and 302–309.

[5] S. Datta and B. J. Hunsinger, J. Appl. Phys. 50, 5661 (1979).

[6] Reference 4, pp. 280–282.

[7] S. Ramo, J. R. Whinnery, and T. Van Duzer, *Fields and Waves in Communication Electronics* (Wiley, New York, 1965), p. 605.

APPENDIX D

SAW RESONATORS ON SILICON WITH ZnO LIMITED TO IDT REGIONS

S. S. Schwartz, S. J. Martin,* R. L. Gunshor, S. Datta, and R. F. Pierret

School of Electrical Engineering, Purdue University
West Lafayette, Indiana 47907

Abstract

Surface acoustic wave resonators with ZnO limited to IDT regions are presented for an externally coupled resonator configuration. The reflection from gratings consisting of grooves in both silicon and SiO_2 is discussed. Externally coupled resonators with reflective gratings consisting of grooves etched in unoxidized silicon are found to exhibit Q-values in excess of 20,000.

I. Introduction

Surface acoustic wave resonators have been adapted to the $ZnO/SiO_2/Si$ layered medium configuration and have previously been constructed using reflector arrays of both isolated and shorted metal strips on the surface of the ZnO as well as grooves milled into the ZnO layer. Martin et.al.[1] have shown that the groove reflector technique yields resonators which have Q values of the order of 10,000. In this paper we present resonators which consist of ZnO deposited only in the transducer regions and reflector arrays of grooves milled into either SiO_2 or silicon. ZnO Resonators fabricated utilizing this method have displayed Q values 70% higher than previously obtained. Besides increasing the Q of the resonator, an additional benefit of this type of resonator is that there is a minimum amount of chip area that needs to be exposed to ZnO sputtering damage.

Resonators constructed in the $ZnO/SiO_2/Si$ layered configuration have exhibited favorable ageing characteristics and have been fabricated with temperature stability which is competitive with that of quartz resonators.[2] The motivation behind using silicon substrates lies in the possibility of incorporating these devices as on-chip, rather than discrete circuit components as well as the fact that fabrication techniques are compatible with those of current integrated circuit fabrication technology.

Advantages associated with this device structure, where the ZnO underlies only the transducers are presented in section II. The reflectivity of grooves in ZnO, SiO_2, and silicon are presented in section III followed by experimental results which appear in section IV. Fabrication techniques associated with this device configuration are considered in section V.

* Present address: Sandia Laboratories, Albuquerque, New Mexico

II. Device Structure

A schematic of the externally coupled ZnO resonator having etched groove reflectors in SiO_2 is shown in Figure 1. One will note the transducer regions are the only places where ZnO is to be found. These ZnO regions can be defined either by chemically etching the ZnO layer or by using a shield during the sputtering process. An advantage of the latter technique is that sputtering damage can be restricted to a minimum area of the wafer.

A feature associated with the growth of thin films is the possibility of some nonuniformity in thickness over a sample. In fabricating resonators using etched grooves in the ZnO layer, it is important to maintain good control of the film thickness in the grating region; this is especially important due to the velocity gradient associated with a change in film thickness of the dispersive ZnO layer. The velocity gradient can both degrade the reflection magnitude and increase the bandwidth of a reflective array. The nonuniformity problem is alleviated in devices constructed using grooves in silicon or grooves in SiO_2 where the dispersion is considered negligible.

Perhaps the most important reason for employing the proposed configuration without ZnO in the reflector grating region is to reduce propagation loss associated with the ZnO film. Resonators constructed using grooves etched in the ZnO layer exhibit Q values which are limited by propagation loss in the ZnO. By elimination of the ZnO layer in the grating regions, one anticipates a significant improvement in Q. Propagation loss is related to Q via the relationship,

$$Q = \frac{\pi}{\alpha \lambda} \qquad (1)$$

where α is the propagation loss per unit length and λ is the wavelength.
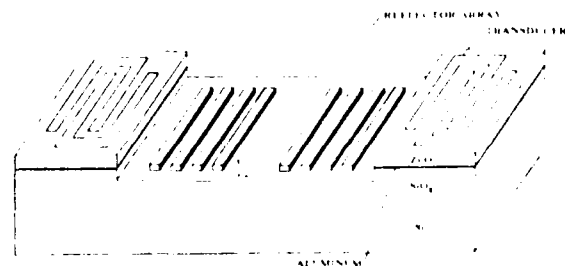

Fig. 1. Externally coupled SAW resonator employing reflective gratings of grooves etched into SiO_2 and ZnO limited to the transducer regions.

III. Reflector Array Characteristics

A series of experiments involving the measurement of the transmission through reflector arrays of 400 ion-milled grooves were performed to determine the reflectivity per groove for various values of groove depth. A plot of reflectivity per periodic section versus normalized groove depth, hk, is shown in Figure 2. Experimental points together with a theoretical curve for grooves both in silicon and SiO_2 indicate that experimental results appear to be in close agreement with theory.[3,4] Also included in the figure is a line showing experimental reflectivity data for grooves etched into the surface of a 0.7 μm ZnO film on 3.05 μm SiO_2 as previously reported.[5] All measurements and predictions are for (111) cut $<2\bar{1}\bar{1}>$ propagation direction silicon substrates. Clearly, by elimination of the ZnO layer in the grating region, one must use deeper grooves, more reflectors, or a combination of these two to obtain the same amount of reflection from a grating etched into silicon or SiO_2. An increase in the groove depth will eventually decrease Q due to scattering into bulk modes, whereas an increase in the number of reflectors per grating will increase the effective cavity length and hence, raise the Q at the expense of an increased device size.
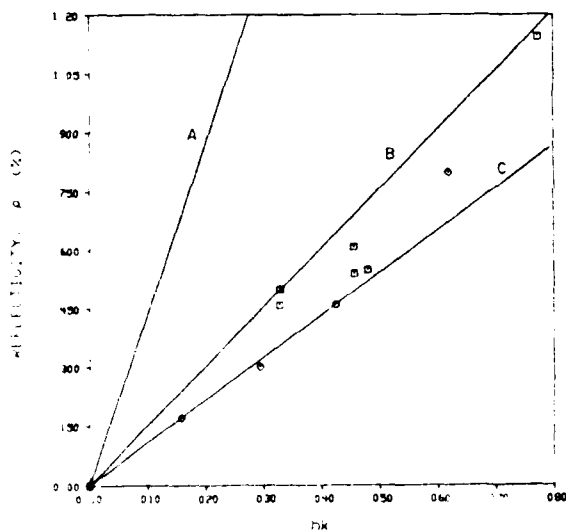

Fig. 2 Reflectivity per groove vs. normalized groove depth for the following configurations:
A) Grooves in 0.7 μm ZnO on 3.05 μm SiO_2,
B) Grooves in 3.05 μm SiO_2,
C) Grooves in unoxidized silicon.
All substrates are (111) cut silicon, $<2\bar{1}\bar{1}>$ propagation direction.

IV. Experimental Results

The transmission response of an externally coupled resonator constructed with 0.36 μm grooves in unoxidized silicon is shown in Figure 3. The cavity spacing between reflective gratings is 27 wavelengths and the acoustic aperture is 30 wavelengths. The Q of this device is 24,800 which is 70% higher than for a device of equal dimensions fabricated with grooves in ZnO. An
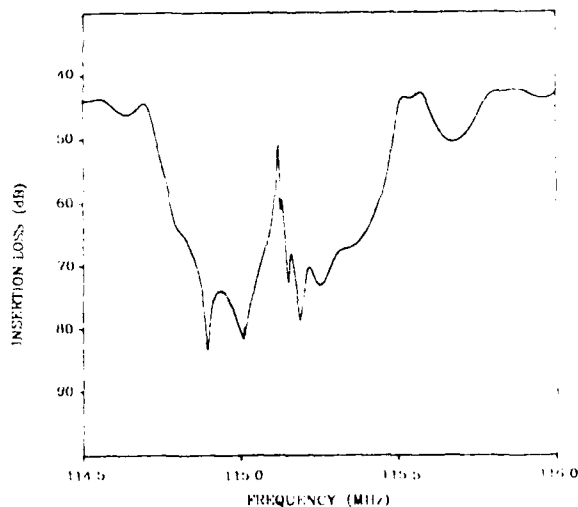

Fig. 3. Transmission response of an externally coupled resonator with 0.36 μm grooves in unoxidized silicon.

externally coupled resonator constructed using grooves in SiO_2 was found to have a Q of 17,400 at 110 MHz.

These results show a significant improvement in Q for the resonator configuration presented compared with those constructed with grooves in the ZnO layer.

Preliminary results for an internally coupled transducer configuration have been examined with ZnO limited to the transducer region. A distinctive feature of this type of resonator is that of an abrupt step at the edge of the transducer region caused by etching away the ZnO. Of course with a thick film one would expect a large reflection from this discontinuity since, to first order, the reflection at such a discontinuity would be proportional to $\frac{h}{\lambda}$, where h is the step height. However, in a device with a ZnO thickness of 0.7 μm and a wavelength of 40.64 μm, $\frac{h}{\lambda} = 0.017$ and calculations [3] predict a reflectivity at the step on the order of four percent.

Measurements on internally coupled resonators indicate that the step is not a major impediment to obtaining acceptable resonator performance in thin film devices; a taper is not required. Several configurations for internally coupled resonators are under examination, and results will be reported in future publications.

V. Fabrication Techniques

Fabrication of the resonators under consideration involves a slightly different procedure than used in previously described on-silicon SAW resonators since the reflective grating and the transducers are no longer in the same plane. The processing steps will be outlined below with the aid of Figure 4.

Step (a): Evaporate a 0.1 μm aluminum layer atop the silicon or SiO_2 layer. The purpose of this layer is to serve as a shorting plane beneath the transducers. This layer enhances $\frac{\Delta v}{v}$ as well as shields the
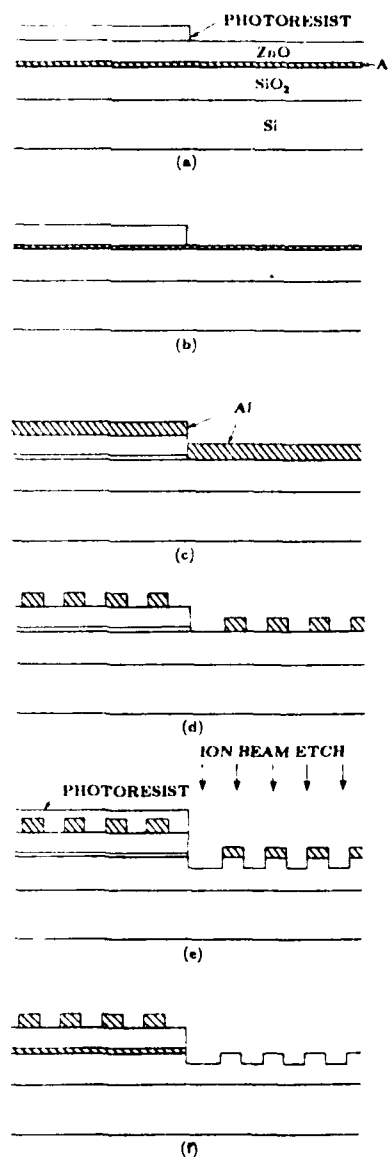
grating). Etch the resonator pattern in the aluminum and strip the photoresist.

Step (e): Cover the transducer regions with photoresist. Boil in de-ionized water for 10 minutes to form an Al_2O_3 layer on the grating aluminum.[6] Etch reflector grooves using an ion milling machine. The purpose of the alumina layer is that alumina etches at a rate approximately four times slower than aluminum, silicon, and SiO_2, which all have comparable etch rates. This is important since deeper grooves are necessary to obtain the same reflectivity for grooves etched in ZnO devices as mentioned earlier. The presence of the alumina, then, allows one to etch deep grooves without an excessively thick aluminum mask.

Step (f): Chemically etch the remaining grating mask material and strip the photoresist.

VI. Conclusions

It has been shown that resonators can be fabricated with ZnO limited to the transducer regions only and that such devices exhibit high Q values for reflector arrays etched in both silicon and SiO_2.

The authors wish to thank Dr. R. Razouk and Marianne Brenner of Fairchild for growing the thick SiO_2 films, and M. Young, T. Miller, and C. Belting for their assistance in the fabrication of these devices.

Fig 4. Fabrication steps for SAW resonators with ZnO only in the transducer regions. Steps (a)-(f) are described in section V above.

mobile charge carriers in the silicon from the electric fields associated with the piezoelectric ZnO layer. Diode sputter a 0.7 μm ZnO film. Cover with photoresist and expose a pattern which leaves photoresist where the transducers will be.

Step (b): Etch away the exposed ZnO using a dilute nitric acid solution and strip photoresist.

Step (c): Evaporate a 0.2 μm layer aluminum over the sample.

Step (d): Spin a layer of photoresist, then expose and develop the resonator pattern (transducers and

References

[1] S. J. Martin, R. L. Gunshor, R. F. Pierret, "Zinc Oxide-on-Silicon Surface Acoustic Wave Resonators," *Appl. Phys. Letts.*, vol. 37, no. 8, p. 200, Oct. 15, 1980.

[2] S. J. Martin, R. L. Gunshor, R. F. Pierret, "High-Q, Temperature Stable ZnO-on-Silicon SAW Resonators," *1980 Ultrasonics Symposium Proceedings*, IEEE Cat. No. 80CH1622-1, p.113.

[3] S. Bandyopadhyay, S. Datta, S. J. Martin, and R. L. Gunshor, "Coherent Mode Conversion by Grooved Arrays in Layered Media," *J. Appl. Phys.*, Jan., 1984, to be published.

[4] S. Datta, "Reflection and Mode Conversion of Surface Acoustic Waves in Layered Media," *1983 Ultrasonics Symp.*, to be published.

[5] S. J. Martin, S. S. Schwartz, R. L. Gunshor, and R. F. Pierret, "Surface Acoustic Wave Resonators on a ZnO-on-Silicon Layered Medium," *J. Appl. Phys.*, vol. 54, no. 2, Feb., 1983, pp. 561-569.

[6] H. Harada, R. L. Gunshor, "Two-Layer Interdigital Transducer for Acoustic-Surface-Wave Devices," *Elect. Letts.*, vol. 12, no. 3, Feb. 5, 1976.

END

FILMED

3-85

DTIC